Modeling Ocean–Cryosphere Interactions off Adélie and George V Land, East Antarctica

KAZUYA KUSAHARA,[a] HIROYASU HASUMI,[b] ALEXANDER D. FRASER,[a,c] SHIGERU AOKI,[c] KEISHI SHIMADA,[d] GUY D. WILLIAMS,[e,a] ROBERT MASSOM,[f,a] AND TAKESHI TAMURA[g,h,a]

[a] *Antarctic Climate & Ecosystems Cooperative Research Centre, University of Tasmania, Hobart, Tasmania, Australia*
[b] *Atmosphere and Ocean Research Institute, The University of Tokyo, Kashiwa, Chiba, Japan*
[c] *Institute of Low Temperature Science, Hokkaido University, Sapporo, Hokkaido, Japan*
[d] *Tokyo University of Marine Science and Technology, Tokyo, Japan*
[e] *Institute of Marine and Antarctic Studies, University of Tasmania, Hobart, Tasmania, Australia*
[f] *Australian Antarctic Division, Kingston, Tasmania, Australia*
[g] *National Institute of Polar Research, Tachikawa, Tokyo, Japan*
[h] *Graduate University for Advanced Studies (SOKENDAI), Tachikawa, Tokyo, Japan*

(Manuscript received 5 November 2015, in final form 29 August 2016)

ABSTRACT

Ocean–cryosphere interactions along the Adélie and George V Land (AGVL) coast are investigated using a coupled ocean–sea ice–ice shelf model. The dominant feature of the Mertz Glacier Tongue (MGT), located at approximately 145°E, was a highly productive winter coastal polynya system, until its calving in February 2010 dramatically changed the regional ''icescape.'' This study examines the annual mean, seasonal, and interannual variabilities of sea ice production; basal melting of the MGT; ice shelves, large icebergs, and fast ice; Dense Shelf Water (DSW) export; and bottom water properties on the continental slope and rise, and assesses the impacts of the calving event. The interannual variability of the winter coastal polynya regime is dominated by the regional offshore winds and air temperature, which are linked to activity of the Amundsen Sea low pressure system. This is the main driver of the interannual variability of DSW exported from the AGVL region. The calving event led to a decrease in sea ice production that resulted in a decrease in the density of DSW export. Subsequently, there is extensive freshening downstream over the continental shelf and slope regions. In addition, it is found that the calving event causes a significant decrease in the mean melt rate of the MGT, resulting from a decrease in ocean heat flux into the cavity due to ocean circulation changes.

1. Introduction

Numerous coastal latent heat polynyas (also known as ''winter coastal polynyas,'' hereafter referred to as ''coastal polynyas'') are present around the Antarctic continent during the freezing season (Massom et al. 1998; Tamura et al. 2008; Kern 2009). Antarctic coastal polynyas are areas of open water and newly formed sea ice adjacent to the coastline or the edges of ice shelves, fast ice, and grounded icebergs. They typically recur on the western side of topographic features, which promote regions of open water by blocking the westward advection of sea ice by the easterly coastal wind regime (Massom et al. 1998; Fraser et al. 2012; Nihashi and Ohshima 2015). Here, large ocean heat losses occur because of the direct contact between the relatively warm ocean surface and the very cold air from the Antarctic continent and ice sheet, resulting in high sea ice production. The associated brine rejection and increase in the density of the ocean surface layer drives the generation of the winter mixed layer, which in highly productive polynya regions can generate cold, saline Dense Shelf Water (DSW) capable of producing Antarctic Bottom Water (AABW). Typical Antarctic water masses on and off the continental shelf region are shown in temperature–salinity space in Fig. 1.

Classically, ice shelf basal melt is related to the depth range, circulation, and melting potential of three key water masses (Jacobs et al. 1992): DSW, modified Circumpolar Deep Water (mCDW), and Antarctic Surface Water (AASW). In highly active polynya regions like

Corresponding author address: Kazuya Kusahara, Antarctic Climate and Ecosystems Cooperative Research Centre, University of Tasmania, Private Bag 80, Hobart TAS 7001, Australia.
E-mail: kazuya.kusahara@gmail.com

DOI: 10.1175/JCLI-D-15-0808.1

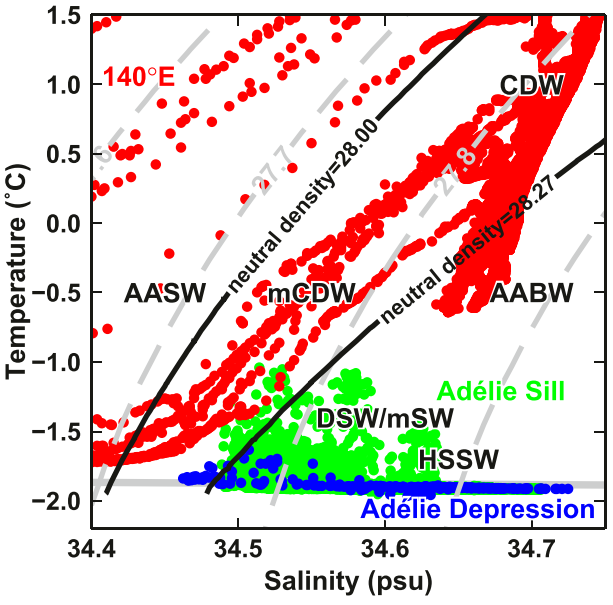

FIG. 1. Temperature–salinity diagram of observations on the continental shelf [blue, data from Williams and Bindoff (2003)], near the Adélie Sill [green, data from Williams et al. (2008)], and along 140°E [red, data from Aoki et al. (2005)]. See blue, green, and red dots in Fig. 2 for the locations. Abbreviations of Antarctic water masses are overlain. CDW indicates Circumpolar Deep Water, mCDW modified CDW, AASW Antarctic Surface Water, AABW Antarctic Bottom Water, mSW modified Shelf Water, DSW Dense Shelf Water, and HSSW High Salinity Shelf Water. Gray dashed contours show the potential density, and black lines show two neutral density surfaces of 28.00 and 28.27 kg m^{-3}. The gray straight line represents the surface freezing points.

Adélie and George V Land (AGVL; see Fig. 2), the DSW can access the ice sheet grounding line where the temperature difference from the pressure-suppressed freezing point drives basal melting. In the AGVL region, DSW is the densest water mass, while mCDW occupies the middepth range below AASW and therefore predominantly interacts with the upper 500 m of the Mertz Glacier Tongue (Williams and Bindoff 2003). Melting at the base of ice shelves supplies fresh and cold glacial meltwater to the water column. The freshening and cooling have opposing buoyancy effects on density (i.e., freshening decreases seawater density). The freshening effect on density is stronger than the cooling effect over Antarctic continental shelves in relevant depth ranges. Therefore, glacial meltwater contributes to upwelling along the ice shelf base, and provides less dense water to the coastal ocean. The increased stratification with the glacial meltwater acts to reduce DSW formation.

At some critical density, DSW has sufficient negative buoyancy relative to the ambient water mass on the continental slope to mix downslope and produce AABW (Williams et al. 2010). In these overflow regions, the modified Shelf Waters (mSW) increase in volume through entrainment of the ambient waters (i.e., mCDW over the continental slope and rise). DSW formation in Antarctic coastal polynyas and subsequent AABW formation over the Antarctic continental slope and rise play crucially important roles in controlling deep thermohaline circulation and structure.

The Mertz Polynya in the AGVL region is known to have been the largest coastal polynya in East Antarctica, dominated by a complex ''icescape'' (Barber and Massom 2007). The Mertz Polynya formed in the lee of the coastline, the Mertz Glacier Tongue (MGT, the floating part of the Mertz Glacier), and a line of small grounded icebergs (Fig. 2; Williams and Bindoff 2003; Lacarra et al. 2011; Dragon et al. 2014). Prior to the calving of the MGT in early 2010, the Mertz Polynya was a persistent coastal polynya in winter and showed very high sea ice production (Tamura et al. 2008). Further, a large depression/trough (the Adélie Depression) exists under the high sea ice production areas, and this topographic feature aids the storage of DSW formed throughout the winter (Williams and Bindoff 2003; Williams et al. 2008). There is also a similar coastal polynya/depression system over the Mertz Depression on the eastern side of the MGT that is also potentially important for the export of DSW, albeit of a less saline variety (Williams et al. 2010). Both depressions have sills across the shelf break to the north, which provide the main pathway for DSW export (Williams et al. 2010).

In February 2010 the MGT calved, resulting from the repositioning of the large iceberg B9B, and this event dramatically altered the icescape in the AGVL region (Legresy et al. 2010). The MGT calving substantially decreased the MGT polynya size and led to a reduced sea ice production (Tamura et al. 2012; Dragon et al. 2014). The reduction of sea ice production and the local melting of a large amount of very thick fast ice resulted in regional freshening just after the calving event and a decrease in seawater density over the Adélie Depression (Shadwick et al. 2013; Lacarra et al. 2014).

Several numerical modeling studies have focused on dense water formation in the Adélie Depression. Marsland et al. (2004) reproduced the MGT coastal polynya system, in terms of its sea ice production and dense water formation over the Adélie Depression, for the first time, using a global coupled ocean–sea ice model. Kusahara et al. (2010, 2011a) showed that a coupled ocean–sea ice model can produce realistic seasonal variations in DSW formation and export. Cougnon et al. (2013) used a regional ocean–ice shelf model to show the impact of basal melting of the MGT on the density of DSW export. Using the ocean–sea ice model

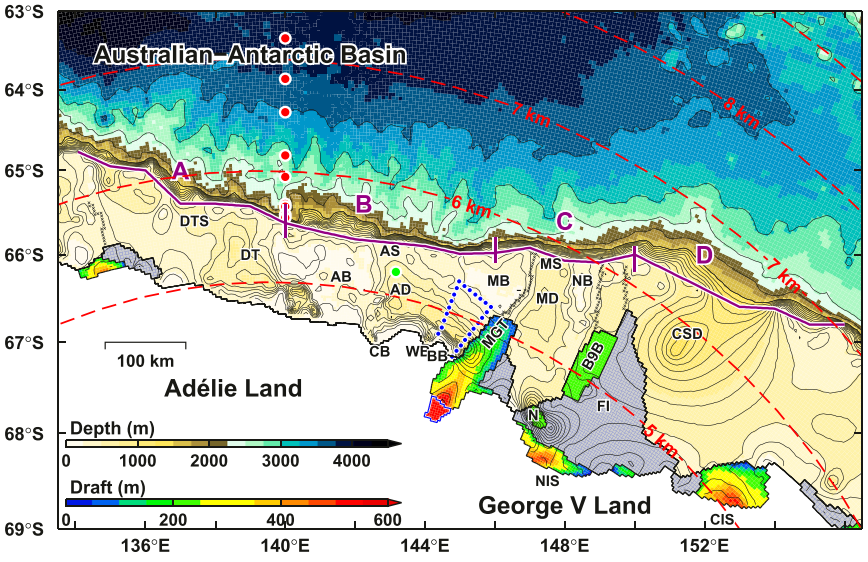

FIG. 2. Bottom topography in the Adélie and George V Land region. Red dashed contours indicate horizontal grid spacing in the model. Gray shaded areas are fast ice with a thickness of 15 m in the model. Purple lines with labels (A–D) indicate the shelf break sections used for the analysis of water exchanges between the continental shelf and slope regions. Black crosses show the specified locations of grounded icebergs. Blue, green, and red dots show the locations for temperature and salinity profiles used in Fig. 1. Black lines shows the depth contour, with 100-m (500 m) intervals in the regions shallower (deeper) than 1500 m. Ice shelves, large icebergs, and fast ice in this figure are shown for the pre-MGT calving configuration (CTRL case). The area enclosed by the blue line indicates the grounding line corrected with interferometric SAR analysis. DT indicates the D'Urville Trough, DTS the D'Urville Trough Sill, AB the Adélie Bank, AS the Adélie Sill, AD the Adélie Depression, CB the Commonwealth Bay, WB the Watt Bay, BB the Buchanan Bay, MB the Mertz Bank, MGT the Mertz Glacier Tongue, MS the Mertz Sill, MD the Mertz Depression, NB the Ninnis Bank, N an iceberg detached from the Ninnis Glacier, NIS the Ninnis Ice Shelf, FI fast ice, CSD the Cook Shelf Depression, and CIS the Cook Ice Shelf.

of Kusahara et al. (2011a), Kusahara et al. (2011b) assessed the impact of the MGT calving event on sea ice production and dense water formation, and showed that the icescape change resulted in a reduction of coastal polynya activity and denser DSW export. Note that in our previous modeling studies (Kusahara et al. 2010, 2011a,b), we did not include ice shelves: regions covered with ice shelves were treated as land grid points. Table 1 is a summary of previous numerical modeling publications for the AGVL region. Although previous works focused on DSW formation over the continental shelf region and export from the shelf break, and some studies investigated the interannual variation in DSW formation, their integration periods are too short to properly investigate interannual variation. Moreover, there has yet to be a modeling study that focuses on the AABW properties over the continental slope and rise downstream of the AGVL region.

In this study, we model all key processes in and around the AGVL region in a single model: notably, sea ice production in coastal polynyas, basal melting of ice shelves/large icebergs/fast ice, DSW formation and export over continental shelf regions, and AABW distribution over continental slope and rise regions. This comprehensive study fills the gaps in previous modeling studies (Table 1).

2. A coupled ocean–sea ice–ice shelf model

This study used a coupled ocean–sea ice–ice shelf model that was utilized by Kusahara and Hasumi (2013, 2014). The model used an orthogonal, curvilinear, horizontal coordinate system. Two singular points of the horizontal curvilinear coordinate were placed on the Indonesian Archipelago (18°S, 130°E) and the East Antarctic Ice Sheet (72°S, 140°E) to regionally enhance the horizontal resolution around the AGVL region, while keeping the model domain almost global.

The vertical coordinate system of the ocean model was a hybrid of σ and z coordinates; the σ coordinate was applied to the uppermost levels between the free surface and 15 m below the mean surface level to avoid

TABLE 1. Foci of previous ocean modeling studies in the Adélie and George V Land region. M2004 indicates Marsland et al. (2004); M2007, Marsland et al. (2007); K2010, Kusahara et al. (2010); K2011A, Kusahara et al. (2011a); K2011B, Kusahara et al. (2011b); C2013, Cougnon et al. (2013); K2013, Kusahara and Hasumi (2013); and S2016, Schodlok et al. (2016); an em dash (—) means not available.

	Annual	Seasonal	Interannual	Calving
Sea ice (ice production)	M2004 K2010 K2011A	M2004 K2011A	M2004 M2007	K2011B
Ice shelf (basal melting)	K2013 C2013 S2016	—	C2013	—
Water masses (dense shelf water)	M2004 M2007 K2010 K2011A K2011B C2013	M2004 K2011A C2013	M2004 M2007	K2011B
Water masses (AABW)	—	—	—	—

outcropping of surface layers, and the z coordinate was applied below that. The vertical grid spacing in the z-coordinate region was 5 m (1 grid) immediately below the σ coordinate and 20 m (99 grids) in depth range from 20 to 2000 m. Below 2000 m, we used 60 grids at a spacing of 50 m. The maximum ocean depth in the model was set to 5000 m to save computational resources. The ice shelf component was only applied over the z-coordinate region. A partial step representation was adopted for both the bottom topography and ice shelf draft to represent them optimally in the z-coordinate ocean model (Adcroft et al. 1997).

The sea ice component used one-layer thermodynamics (Semtner 1976) and a two-category ice thickness representation (Hibler 1979). Prognostic equations for momentum, mass, and concentration were taken from Mellor and Kantha (1989). Internal ice stress was formulated by the elastic-viscous-plastic rheology (Hunke and Dukowicz 1997) and sea ice salinity was fixed at 5 psu.

In the ice shelf component, we assumed a steady shape in the horizontal and vertical directions. The freshwater flux at the base of ice shelves was calculated with a three-equation scheme, based on a pressure-dependent freezing point equation and conservation equations for heat and salinity (Holland and Jenkins 1999). This model was not eddy-resolving and did not include tidal forcing, and thus we used the velocity-independent coefficients for the thermal and salinity exchange velocities (i.e., $\gamma_t = 1.0 \times 10^{-4}$ and $\gamma_s = 5.05 \times 10^{-7}$, respectively; Hellmer and Olbers 1989). This is equivalent to assuming a mixed layer velocity of about 20 cm s^{-1} under the ice shelves. The modeled meltwater flux and the associated heat flux were imposed on the ice shelf–ocean interface.

The ocean model included a uniform third-order polynomial interpolation algorithm for tracer advection (Leonard 1993), isopycnal diffusion with a coefficient of 1.0×10^1 m^2 s^{-1}, isopycnal layer thickness diffusion with a coefficient of 1.0 m^2 s^{-1} (Gent et al. 1995), and a surface mixed layer parameterization based on turbulence closure (Noh and Kim 1999). Under the ice shelves, the surface mixed layer parameterization was neglected.

The horizontal grid spacing over the AGVL region was less than 7 km (Fig. 2). This relatively high horizontal resolution enabled the simulation to produce high sea ice production and dense water formation along the Antarctic coastal margins (Marsland et al. 2004; Kusahara et al. 2010, 2011a). The global bathymetry for the model was derived from the General Bathymetric Chart of the Oceans (GEBCO; IOC et al. 2003), while ice shelf draft and bathymetry under the ice shelf were obtained from the 1-min refined topography (RTopo-1) dataset (Timmermann et al. 2010).

The drafts of large grounded icebergs (B9B and an iceberg detached from the Ninnis Glacier; Massom 2003) were set to 200 m. In reality, these large icebergs are grounded somewhere at the base. However, we prescribed that these icebergs are afloat, as with ice shelves, because there is no accurate information about the icebergs' draft and a small water column thickness between the sea floor and the iceberg base near the grounding position leads to numerical instability. In our previous models (Kusahara et al. 2010, 2011a,b), the large icebergs were treated as land grid points. Although we are not sure which treatment is better, in this study the afloat approximation was used to estimate ocean–large iceberg interaction. The grounding line of the MGT was estimated by interferometric synthetic aperture radar (SAR) analysis using *ERS-1* and *ERS-2* satellite data (T. Yamanokuchi 2011, personal communication), and its draft was set to 550 m, which was extrapolated from the draft from Rtopo1 near the grounding line (see the area enclosed by the blue line in Fig. 2). The actual draft near the grounding line is known to be deeper than this (Legrésy et al. 2004; Mayet et al. 2013), and thus the difference may lead our model to underestimate the basal melt rate near the grounding line.

North of 40°S, temperature and salinity were restored to the monthly mean climatology of the *World Ocean Atlas 1998* (Levitus et al. 2013) throughout the water column with a damping time scale of 10 days. Outside of East Antarctica (i.e., west of 50°E and east of 162°E, where the horizontal resolution becomes coarser), sea surface salinity was restored to the monthly mean climatology to suppress unrealistic deep convection in some regions (e.g., Weddell Sea). Daily surface boundary

conditions for the model were surface winds, air temperature, specific humidity, downward shortwave, downward longwave, and freshwater flux. To calculate the wind stress and sensible and latent heat fluxes, we used the bulk formula of Kara et al. (2000). When the surface air temperature was below 0°C, precipitation was treated as snow.

Fast ice is sea ice that is fastened to the Antarctic coastline and edges of ice shelves, large icebergs, and grounded icebergs. Extensive fast ice has been identified along the East Antarctic coast (Fraser et al. 2012; Nihashi and Ohshima 2015). Before the MGT calving event, perennial consolidated fast ice with an estimated thickness of up to 50 m existed on the eastern side of the MGT (Massom et al. 2010), although much of the fast ice in the wider region was likely considerably thinner (Giles et al. 2008). We introduced areas of multiyear fast ice into the model as constant-thickness (15 m) ice shelf grid cells. Although in reality the horizontal distribution and thickness of fast ice vary seasonally and interannually (Fraser et al. 2012), the spatial distribution of multiyear fast ice in the model was assumed to be constant in time as a first approximation. The fast ice in the model had zero salinity, which was a reasonable approximation to an observed low salinity of 1.5 psu for multiyear fast ice (Tang et al. 2007).

Coastal polynya regions can also form on the downwind/downstream side of lines of small grounded icebergs, as well as along coastlines and ice fronts (Massom et al. 1998). We prescribed the grid points with lines of small grounded icebergs by setting the sea ice velocity to zero, to incorporate blocking of sea ice advection by subgrid-scale grounded icebergs in the model (Kusahara et al. 2010). Note that oceanic flow was permitted below these grid cells.

We performed a 40-yr simulation driven by present-day climate conditions, as the CTRL case. Surface boundary conditions were calculated from the atmospheric surface data of ERA-Interim (Dee et al. 2011). Initial values of temperature and salinity were derived from the January climatology of the *World Ocean Atlas 1998* (Levitus et al. 2013) and the ocean velocities were initially set to zero. We integrated the model for the first five years using the 1979 forcing repeatedly to spin up the sea ice fields. Subsequently, we performed a hindcast simulation for the period 1979–2013.

We also performed numerical experiments for the postcalving configuration in which we assumed that a portion of the floating part of the MGT, large icebergs, and extensive fast ice on the eastern side of the MGT instantly disappeared. We conducted two experiments in which the calving event was assumed to occur on 1 January of 2010 and 2000 (the C2010 and C2000 cases). The initial conditions of the two experiments were derived from the results in the CTRL case. Although the icescape configurations were largely simplified compared to the actual time-varying settings (including the precalving period), dynamical interpretation is more straightforward using this approximation. The C2000 case was conducted to understand how quickly the systems change after the instantaneous icescape change by comparison with the C2010 case and to show that the numerical results are independent of the timing of the calving event. Moreover, the results from the C2000 case were utilized to obtain better long-term-averaged fields without the biases that come from interannual variability.

3. Annual/mean state and seasonal variation in the precalving configuration

Before examining the interannual variability and impacts of the icescape change on the physical ice and ocean systems, we describe the model representations of the annual/seasonal fields of 1) sea ice production; 2) basal melting of ice shelves, large icebergs, and fast ice; and 3) the ocean structures around the AGVL region. Here, we compare the model results from the CTRL case (i.e., the precalving configuration) for each component with satellite-based estimates, in situ observations, and previous modeling studies to assess the model's performance.

a. Annual sea ice production

Active sea ice production areas ($>20\,\mathrm{m\,yr^{-1}}$) are reproduced in the model in coastal regions east of 140°E, on the western side of the MGT, and west of the "dagger" of small icebergs (Fig. 3). The magnitude of ice production exponentially decays from the coastline or ice front, with a typical decay scale distance of 100 km. There is another area of active sea ice production, with production higher than $15\,\mathrm{m\,yr^{-1}}$, south of the Mertz Depression. The modeled spatial distribution of high sea ice production over the Adélie and Mertz Depressions is largely consistent with satellite-based estimates (Tamura et al. 2008, 2012). Total annual mean sea ice production over the Adélie and Mertz Depressions (areas enclosed by gray line and lines of small grounded icebergs in Fig. 2) for the period 1979–2013 in the model is 204 ± 16 and $92 \pm 13\,\mathrm{km^3\,yr^{-1}}$, respectively. The model estimates are higher than the estimates from Tamura et al. (2008) for the period 1992–2009 (Adélie Depression: 139 ± $21\,\mathrm{km^3\,yr^{-1}}$; Mertz Depression: 53 ± $12\,\mathrm{km^3\,yr^{-1}}$). However, the algorithm for the satellite-based estimate is tuned for thin ice areas (Tamura et al. 2008), and the observed sea ice production in the offshore areas could be underestimated (Kusahara et al. 2010). Taking

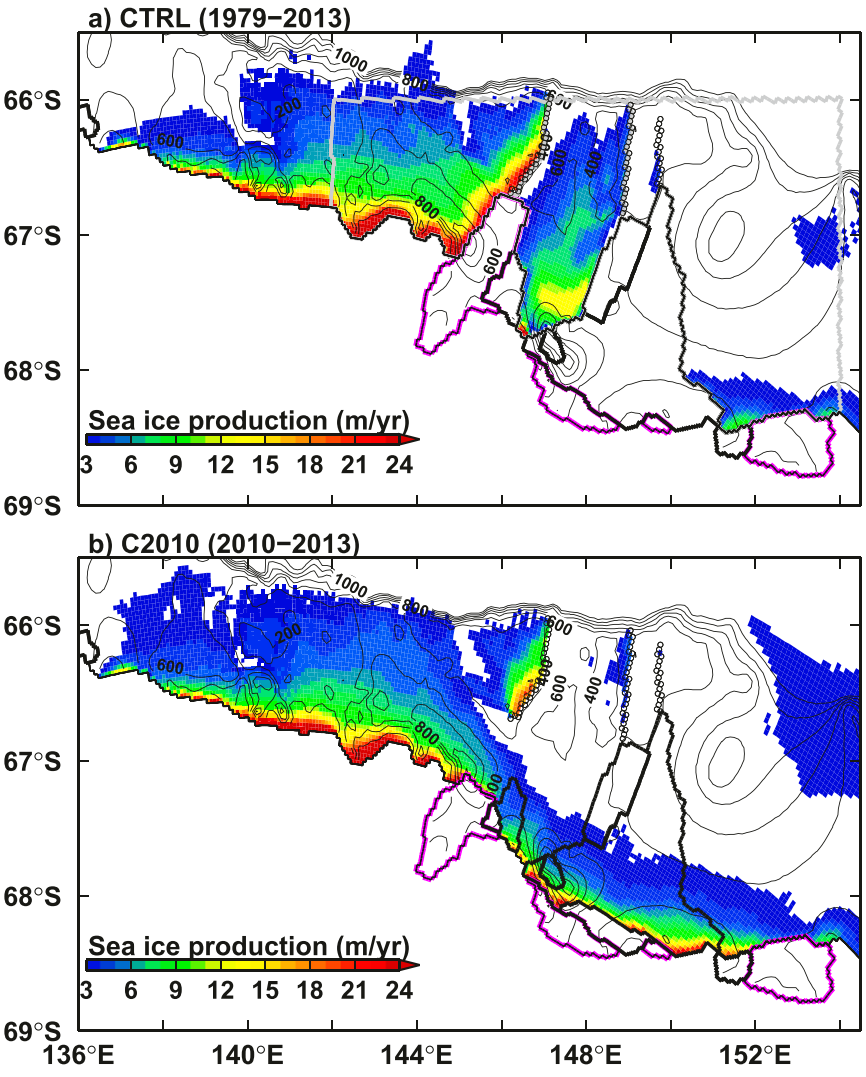

FIG. 3. Maps of mean annual sea ice production (m yr^{-1}) (a) before and (b) after the calving of the Mertz Glacier Tongue. The sea ice production in the CTRL and C2010 cases were averaged over 1979–2013 and 2010–13, respectively. Purple lines show the boundaries of the ice shelf regions. Areas of sea ice production below 3 m yr^{-1} are masked out. Thick black lines show boundaries of icebergs and fast ice before the MGT calving. Black circles show the locations of grounded icebergs, which block sea ice advection. The contours show the depth, with 200-m intervals in regions shallower 1000 m. Gray lines indicate the boundaries used for calculating sea ice production.

account of these circumstances, the modeled sea ice production over the AGVL region shows reasonable agreement with observational estimates, providing confidence in this model's ability to reproduce regional ocean–sea ice interaction.

b. Basal melting at ice shelves and fast ice

The annual basal melt rate and amount at ice shelves and fast ice in the model is summarized in Table 2. Active basal melt rates higher than 5 m yr^{-1} are produced on the western part of the MGT (Fig. 4a). The total basal melt of the MGT is estimated to be 17.0 Gt yr^{-1}, which is larger than recent observational estimates [7.9 Gt yr^{-1} in Rignot et al. (2013) and 5 Gt yr^{-1} in Depoorter et al. (2013)]. Previous observational estimates range from 5 to 44 Gt yr^{-1}, with a wide range of basal melt rate (0.87–18 m yr^{-1}; Table 3).

The average basal melt rate of fast ice, 0.46–1.47 m yr^{-1}, is smaller than that of the ambient ice shelves and large icebergs; however, the fast ice melt amount accounts for 27% of the total melt from ice shelves, icebergs, and fast ice, due to its large areal extent. This result suggests that extensive melting of fast ice strongly contributes to the

TABLE 2. Mean and interannual standard deviation of basal melt amount and rate of ice shelves, large icebergs, and fast ice at the features (A–I) labeled in Fig. 4. The basal melting amount and rate are calculated from the water flux with an assumption of a seawater density of 1028 kg m^{-3} and an ice shelf density of 917 kg m^{-3}. NIS is the Ninnis Ice Shelf and CIS the Cook Ice Shelf.

		CTRL (1979–2013)			C2010 (2010–13)		
Label	Name	Area (km^2)	Amount (Gt yr^{-1})	Rate (m yr^{-1})	Area (km^2)	Amount (Gt yr^{-1})	Rate (m yr^{-1})
A (A′)	MGT	5887	17.0 ± 2.52	3.14 ± 0.47	3518	3.1 ± 1.13	0.95 ± 0.35
B (B′)	Fast ice	1353	1.8 ± 0.57	1.47 ± 0.45	256	0.1 ± 0.06	0.22 ± 0.24
C	Iceberg	405	0.9 ± 0.17	2.43 ± 0.47	—	—	—
D	NIS (west)	1761	3.9 ± 0.74	2.43 ± 0.46	1761	2.7 ± 0.27	1.69 ± 0.16
E	B9B	2710	7.9 ± 1.90	3.18 ± 0.77	—	—	—
F (F′)	Fast ice	15323	11.0 ± 5.00	0.78 ± 0.35	1468	0.3 ± 0.07	0.22 ± 0.05
G	NIS (east)	246	0.2 ± 0.05	0.86 ± 0.24	246	0.2 ± 0.01	0.78 ± 0.04
H	Fast ice	678	0.3 ± 0.18	0.46 ± 0.29	678	0.1 ± 0.03	0.15 ± 0.05
I	CIS	3483	5.3 ± 1.40	1.66 ± 0.44	3483	4.0 ± 0.20	1.24 ± 0.06

regional freshwater input over the AGVL region. Annual precipitation on the fast ice in this region is estimated to be about 65 cm yr^{-1} water equivalent (1979–2013 average in the ERA-Interim dataset). The precipitation is insufficient to sustain the active melting fast ice. In reality, much of the fast ice in this region is formed by dynamical interactions between advected sea ice and coastal protrusions, such as the coastline, ice front, or small icebergs (Fraser et al. 2012), and is heavily deformed by dynamic interactions (Massom et al. 2010). The modeled basal melt rates of the fast ice are achievable if there is enough input from advected sea ice. It is, however, difficult to estimate the contribution of advected pack ice to the mass balance of the fast ice.

The area-averaged basal melt rate of the MGT is at its maximum in summer and minimum in winter (Fig. 5), as modeled for total melting of Antarctic ice shelves by Dinniman et al. (2015). The interannual variation of the monthly basal melt rate (shown as error bars) is largest in summer and smallest in winter. As explained later in this section, cold water formed in the coastal polynya dominates the water masses flowing into the MGT cavity every winter, regulating the basal melt to its minimum rate. On the other hand, in summer, interannually variable warm water intrusions from the shelf break bring a large amount of heat onto the continental shelf, resulting in the higher and more variable basal melt rates. Areas of large seasonal basal melt difference are produced on the western side of the ice shelves, icebergs, and fast ice, and the maximum basal melt rate occurs from December to March (Fig. 6). These spatial distributions of basal melt rate difference and peak month coincide with the timing of warm water intrusions onto the continental shelf region.

Floating ice shelves melt at the base due to the input of thermal energy from the ocean (Jacobs et al. 1992). Here, we focus on the water masses flowing into the MGT cavity across the ice shelf edge to examine the oceanic heat input and its seasonality. In the CTRL case (Fig. 5c), relatively warm waters with temperatures of −1.6° to −0.4°C are transported into the MGT cavity during summer (December–March), resulting in high basal melt rates from the MGT (Fig. 5a). From June to October, colder waters with surface freezing point temperatures dominate the water masses flowing into the cavity, resulting in lower basal melt rates. The warm waters during summer originate from AASW and mCDW intrusions onto the continental shelf, crossing the Adélie Sill (Fig. 7a). Vertical profiles of temperature and potential density along the southwestern flank of the Mertz Bank (i.e., along the center of the intrusion) in both summer and winter are shown in Fig. 8. Water with temperatures higher than 0.0°C is present over the continental slope region, and the subsurface temperature maximum is found at a depth range of 50 to 200 m in summer and at approximately 150 m in winter. In summer, there is strong stratification of salinity and density in the surface 50–100-m layer (Fig. 8a). Although the subsurface temperature gradually decreases from the Adélie Sill to the MGT, the water under the MGT in summer is warm enough to melt it. When compared to observed summer water properties over the southwestern flank of the Mertz Bank (Lacarra et al. 2011), the boundary between AASW and mCDW is less clear in the model due to an overestimate of AASW, noting that the modeled intrusion of the temperature maximum is shallower than the observed one. In winter, the model does reproduce the mCDW intrusion at intermediate depths (Kusahara et al. 2011a), and cold water dominates the water column in the coastal region (Fig. 8b).

c. *Dense shelf water export across the shelf break*

Vertical profiles of temperature, salinity, potential density, and ocean velocity along the shelf break

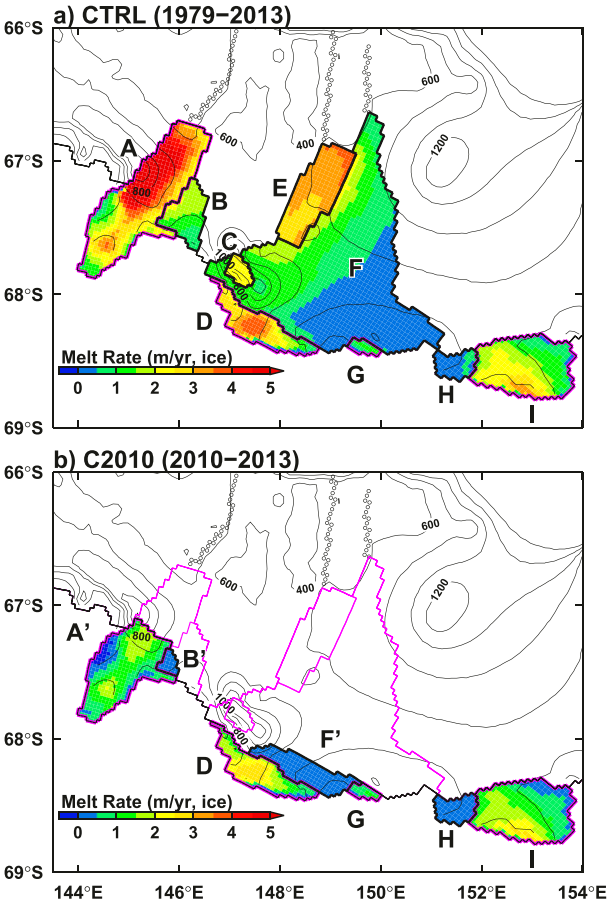

FIG. 4. Maps of annual basal melting (m yr^{-1}) of ice shelves, large icebergs, and fast ice in the CTRL and C2010 cases (see also Table 2). The basal melt rate is calculated from the water flux with an assumption for the seawater density of 1028 kg m^{-3} and an ice shelf density of 917 kg m^{-3}. The sea ice production in the CTRL and C2010 cases was averaged over 1979–2013 and 2010–13, respectively. Contours show the depth, with 200-m intervals in regions shallower than 1000 m. Ice shelves, icebergs, and fast ice with labels A–I are used in Table 2. Purple lines in (b) show the boundaries of icebergs and fast ice in the precalving configuration.

between 134° and 156°E are shown in Fig. 9 for September and Fig. 10 for February. The shelf break is defined as the 500-m depth contour (purple line in Fig. 2). The ocean velocity in Figs. 9 and 10 indicates the component normal to the tangential line of the shelf break, and positive values indicate an offshore direction.

DSW is exported from the AGVL region during winter from three areas (Fig. 9): The Mertz Sill/Bank, the Adélie Sill/Bank, and the sill in the D'Urville Trough (hereafter called the D'Urville Trough Sill). DSW is characterized by high salinity and low temperatures near the surface-freezing point. The densest and coldest DSW export is found near the Adélie Sill/Bank. The salinity of the DSW is higher than 34.7 psu, its

TABLE 3. Comparison of ice shelf basal melting with previous studies for the Mertz Glacier Tongue (MGT) in the precalving configuration. In the method column, O stands for oceanographic estimate, S satellite estimate, CM a circumpolar model, and RM a regional mode.

MGT	Amount	Rate	Method
Observation	(Gt yr^{-1})	(m yr^{-1})	
Bindoff et al. (2001)	44	—	O
Rignot (2002)	—	18	S
Berthier et al. (2003)	—	11	S
Rignot et al. (2013)	7.9	1.4	S
Depoorter et al. (2013)	5	0.87	S
Ocean–ice shelf models	(Gt yr^{-1})	(m yr^{-1})	
This study	17.0	3.14	CM with a regional focus
Kusahara and Hasumi (2013)	7.8–10.7	1.07–1.46	CM
Cougnon et al. (2013)	11.4	1.9	RM
Schodlok et al. (2016)	7.4–13.4	1.28–2.32	CM

temperature is close to the surface-freezing point, and the potential density near the seafloor reaches 27.90 kg m^{-3}. The dense DSW signature spreads extensively between 141° and 143.5°E. The temperature of the DSW export from the Mertz Sill/Bank is at approximately −1.5°C, warmer than that from the Adélie Sill/Bank, and its potential density is closer to 27.85 kg m^{-3}. The features of the DSW export reproduced in the Adélie and Mertz sill regions in this model are consistent with previous observational and modeling studies (Williams et al. 2010; Kusahara et al. 2011a). There is one additional region of active DSW export from the D'Urville Trough Sill, located farther west of the Adélie Bank. In summer, when the export of DSW from the Adélie Sill/Bank and Mertz Sill/Bank substantially decreases, export from the D'Urville Trough Sill is still active (Fig. 10).

Next, the seasonal cycle of DSW export is examined (Fig. 11). The shelf break line is divided into four sections (sections A–D; see Fig. 2). Here, DSW is defined as water masses with potential density higher than 27.84 kg m^{-3} and potential temperature lower than −0.5°C. No DSW export is observed from section D. DSW export across section B (the Adélie Sill/Bank) starts to increase from May, reaches a maximum in September, and then substantially decreases in November–December and is almost zero from January to April. DSW export from section C (the Mertz Sill/Bank) shows a similar seasonal cycle, but the DSW density is lower than that from section B, in agreement with Williams et al. (2010). In section A (the D'Urville Trough Sill), DSW export with a maximum potential density of 27.90 kg m^{-3} is found from winter to spring. The export from section A reaches its maximum in November and its minimum in June. The peak month in section A is delayed by two months

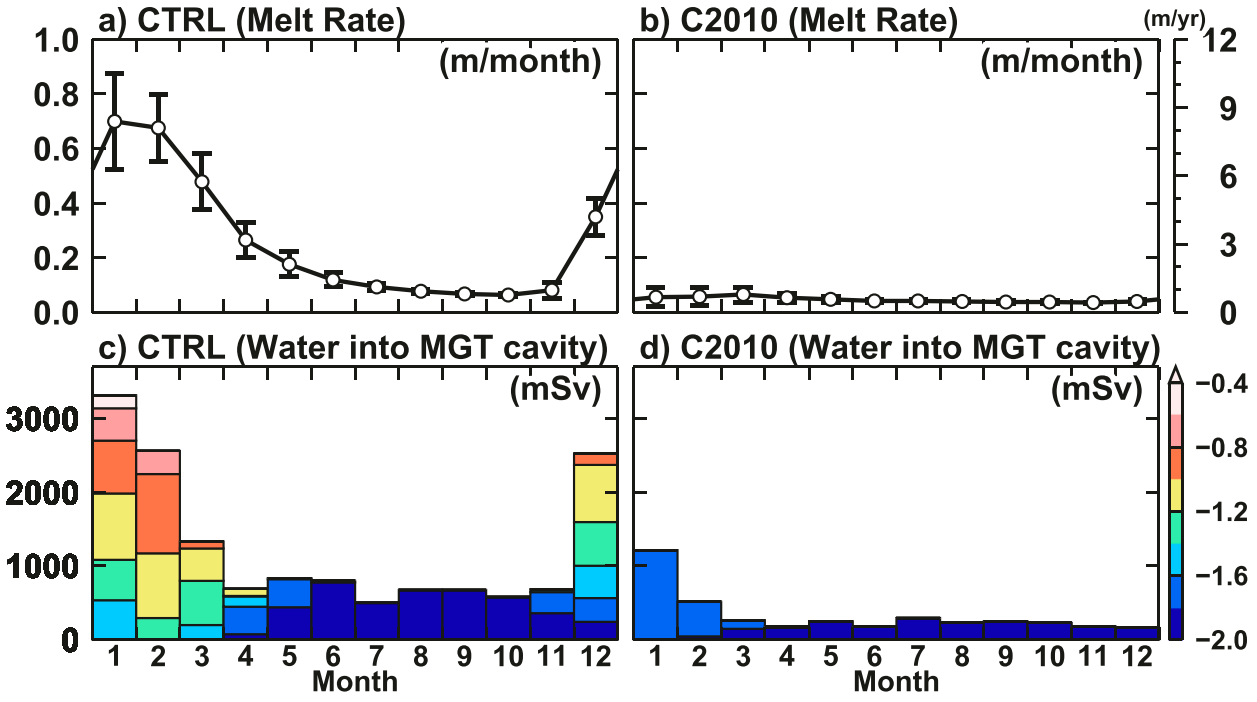

FIG. 5. Seasonal variation of (a),(b) basal melt rate at the MGT and (c),(d) water transport into the MGT cavity, for the (left) CTRL and (right) C2010 cases. Error bars in the top indicate one standard deviation of interannual variability of the monthly basal melt rate over each integration period (1979–2013 and 2010–13). A scale next to (b) is equivalent annual melt rate (m yr^{-1}). Color in the bottom represents water temperature (°C).

relative to that in section B. However, there is no significant sea ice production over the D'Urville Trough. An examination of seasonal bottom salinity over the continental shelf shows the propagation of a high salinity anomaly from the Adélie Depression to the D'Urville Trough (not shown). This indicates that DSW export from section A is related to sea ice production over the Adélie Depression, and that the time lag of two months corresponds to the advection time scale.

d. Antarctic Bottom Water over the continental slope and rise

Modeled vertical profiles of annual mean temperature and salinity along 140°E are shown in Fig. 12. Water properties observed in 1994 (Aoki et al. 2005) are subsampled and overlain on the figure, as colored dots. Looking at the vertical profile of the modeled temperature (Fig. 12a), there is a subsurface maximum at a depth of 200 to 800 m north of 62°S, with waters warmer than 2°C. The temperature maximum corresponds to the center of Upper Circumpolar Deep Water. The central depth of the modeled temperature maximum (red line in Fig. 12a) is at 300-m depth at 62°S and becomes shallower toward the coastal region. This tendency is reversed around 64°S, where the depth of the modeled temperature maximum deepens toward the coast. A potential temperature of 0.0°C is often used as an upper boundary of the AABW over the deep ocean. The thickness of waters colder than 0.0°C in the model is approximately 1000 m, and the waters colder than 0.0°C over the deep ocean are directly connected to the continental shelf region, where the temperature is close to the surface freezing point. Note that the initial condition dataset does not resolve the regional frontal structure over the continental slope and rise regions due to the coarse horizontal resolution (1°), and therefore the structure in Fig. 12 is produced by the internal physics of the model. Observed bottom temperatures are lower than −0.4°C over the lower continental slope and rise. Here, the model reproduces water masses colder than 0.0°C, but the minimum temperature is about −0.2°C, which is warmer than that observed. This warm bias exists all along the 140°E section. Next, looking at the vertical profile of the modeled salinity (Fig. 12b), there is a maximum value of 34.7 psu at a depth of 1000 to 2000 m. This modeled salinity maximum corresponds to the center of Lower Circumpolar Deep Water. The salinity core depth is 1700 m in the offshore region (red line in Fig. 12b) and shallows to 800 m toward the coastal region. The vertical profile of salinity in the model is also consistent with the observations. This comparison of water properties indicates that the model does to some

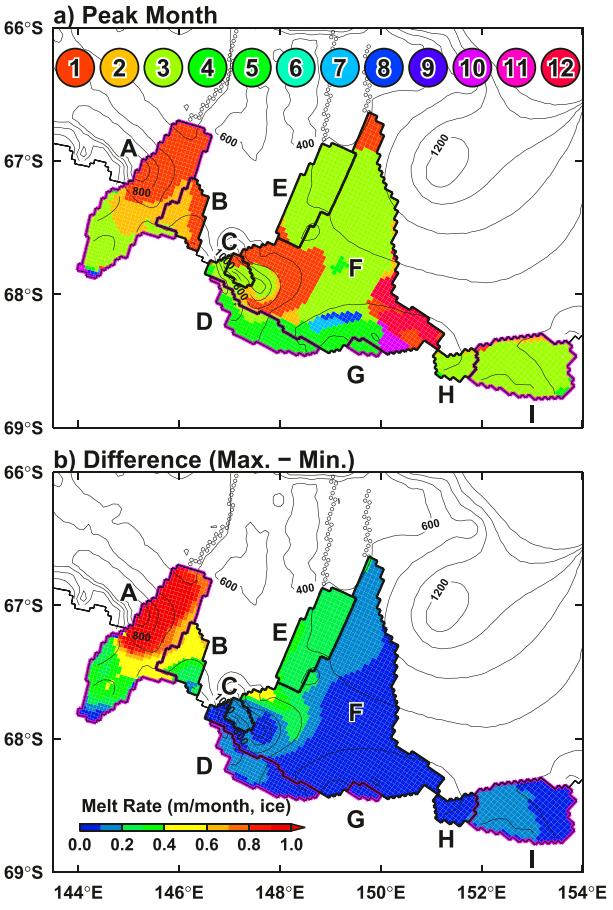

FIG. 6. Maps of (a) peak month of basal melt rate at ice shelves, icebergs, and fast ice and (b) the seasonal difference. The monthly averaged melt rate is based on results from 1979 to 2013. Contours indicate the water depth with an interval of 200 m. Labels A–I are used in Table 2.

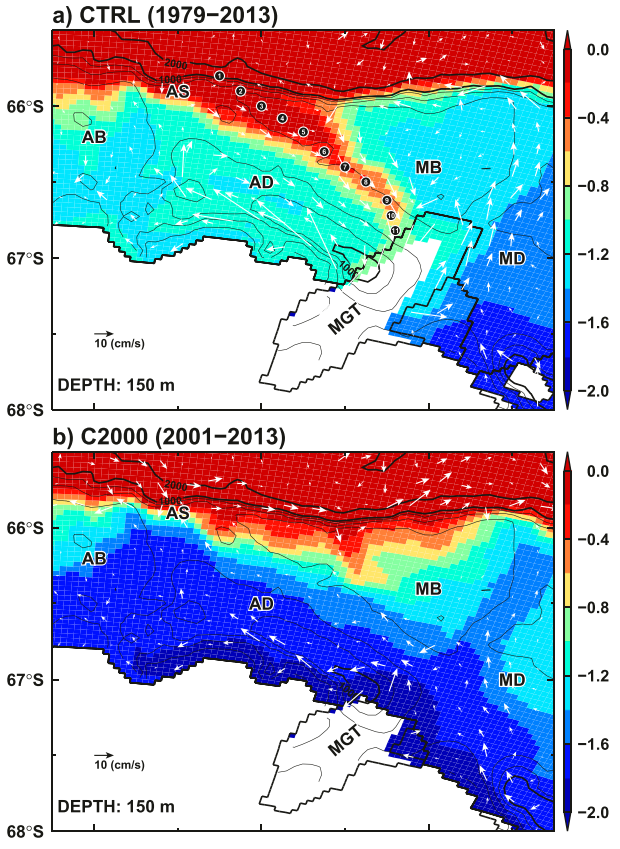

FIG. 7. Horizontal distributions of ocean potential temperature (°C) and velocity (cm s^{-1}) at 150-m depth in summer (averaged over December–March) in the (a) CTRL and (b) C2010 cases. The depth of 150 m approximately corresponds to the draft of the MGT edge. The averaging period is 1979–2013 for the CTRL case and 2001–13 for the C2000 case. Circles with numbers in (a) indicate modeled stations along the southwestern flank of the Mertz Bank to show the modeled vertical sections of temperature and density in Fig. 8.

extent realistically reproduce water masses over the continental slope and rise, although there are differences near the fronts and at the very bottom.

Bottom distributions of modeled mean temperature and its seasonal variation are shown in Fig. 13. Observed temperature from the World Ocean Database 2009 (Boyer et al. 2009) is shown as symbols in Fig. 13a. Note that the timing (month and year) of the observations differs between locations. The horizontal distribution of the bottom temperature and its seasonal amplitude is used to investigate the spreading pathways of newly formed bottom water over the continental slope and rise regions. Since there is a large contrast in temperature between CDW and DSW (Fig. 12a), the potential temperature is useful for tracing AABW. As shown in section 3c (Fig. 9), DSW is being actively exported from the Mertz Sill/Bank, the Adélie Sill/Bank, and the D'Urville Trough Sill (Fig. 13a). Waters colder than −0.4°C are present in the observations just offshore of the Adélie Sill/Bank. The model results are approximately consistent with the observed temperature, in terms of the large-scale temperature contrast between continental slope and deep ocean regions. However, as also shown in Fig. 12, there are strong warm biases in the bottom temperature over the Australian Antarctic basin (see the inset of Fig. 13a).

A large seasonal temperature change is found near the three DSW export regions, showing that DSW overflow occurs seasonally (Fig. 13b), with the strongest signal observed being around the Adélie Sill/Bank. The cold signal from the Adélie Sill/Bank extends into September, consistent with the seasonality of DSW export across the shelf break. It takes about two months for this cold injection from the continental shelf and slope region to reach 3000-m depth and become a source water for AABW.

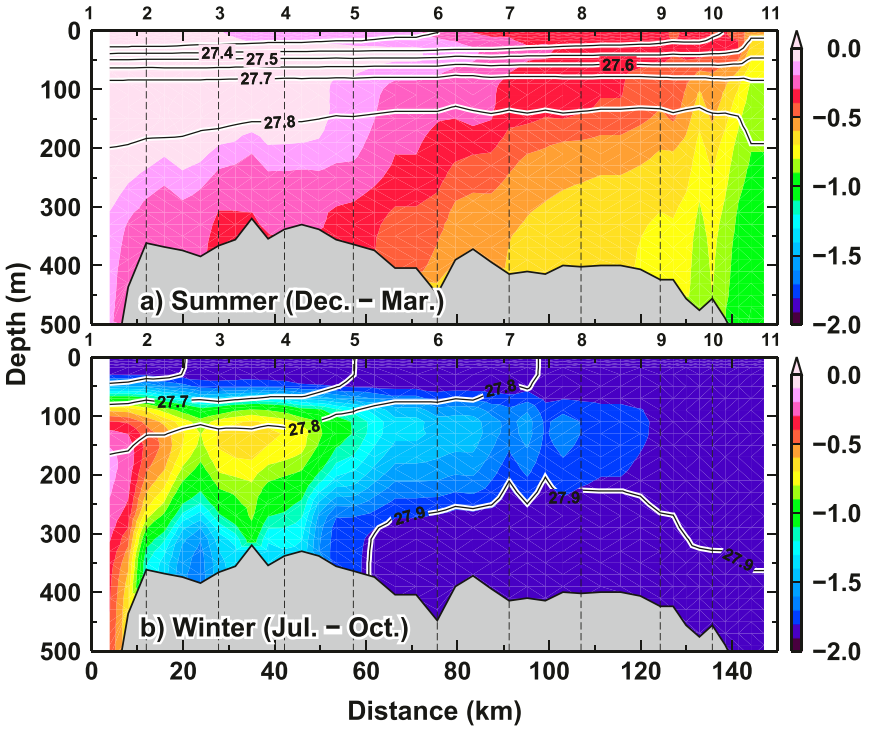

FIG. 8. Vertical sections of potential temperature (°C, color) along the southwestern flank of the Mertz Bank (i.e., the center of the warm water intrusion from the Adélie Sill to the MGT) in (a) summer (averaged over December–March) and (b) winter (averaged over July–October) in the CTRL case (precalving configuration). Potential density anomaly (kg m^{-3}) is shown by contours. The averaging period is 1979–2013. The horizontal axis indicates the distance from station 1 at the shelf break and the numbers on the upper horizontal axis indicate the stations in the model (see the Fig. 7).

4. Interannual variability due to atmospheric forcing

a. Sea ice production

Annual sea ice production over both the Adélie and Mertz Depressions consistently covaries on the scale of years to decades with that of the entire AGVL coastal region (Fig. 14). Henceforth, we focus on the total sea ice production over the AGVL region when investigating the interannual variability. Modeled sea ice production has a decreasing trend before the early 1990s, and subsequently a positive trend. Pronounced interannual variability is present on top of the decadal variability.

A time series of sea ice production estimated from satellite data [updated from Tamura et al. (2008)] also shows a positive trend for the period 1992–2009. The modeled positive trend after the 1990s is consistent with the satellite-based estimate.

Correlation analyses with wind and surface air temperature from 1979 to 2013 reveal that sea ice production over the AGVL region is enhanced by northward winds and colder air temperature (Figs. 15a,b). Atmospheric variables averaged over winter (May–October) are used for the calculations. Offshore winds naturally bring colder air from the Antarctic continent and thus the two atmospheric variables are not completely independent of each other (i.e., both are controlled by large-scale atmospheric phenomena). To illustrate the connection between sea ice production and large-scale atmospheric variability, a correlation map with surface air pressure is shown in Fig. 15c. A significant negative correlation is found over the Amundsen–Bellingshausen Seas, with a pattern that is similar to the Amundsen Sea low (Hosking et al. 2013). In fact, there is a significant negative correlation (−0.49) between AGVL sea ice production and the mean atmospheric sea level pressure averaged around the Amundsen Sea (Fig. 14). Given that the AGVL region is located on the western edge of the Amundsen Sea Low, a stronger Amundsen Sea low leads to enhanced cold northward winds over the AGVL region, giving higher sea ice production in this region.

b. Basal melting of the MGT

In this examination of interannual variability, we define the annual value of basal melting as the sum of

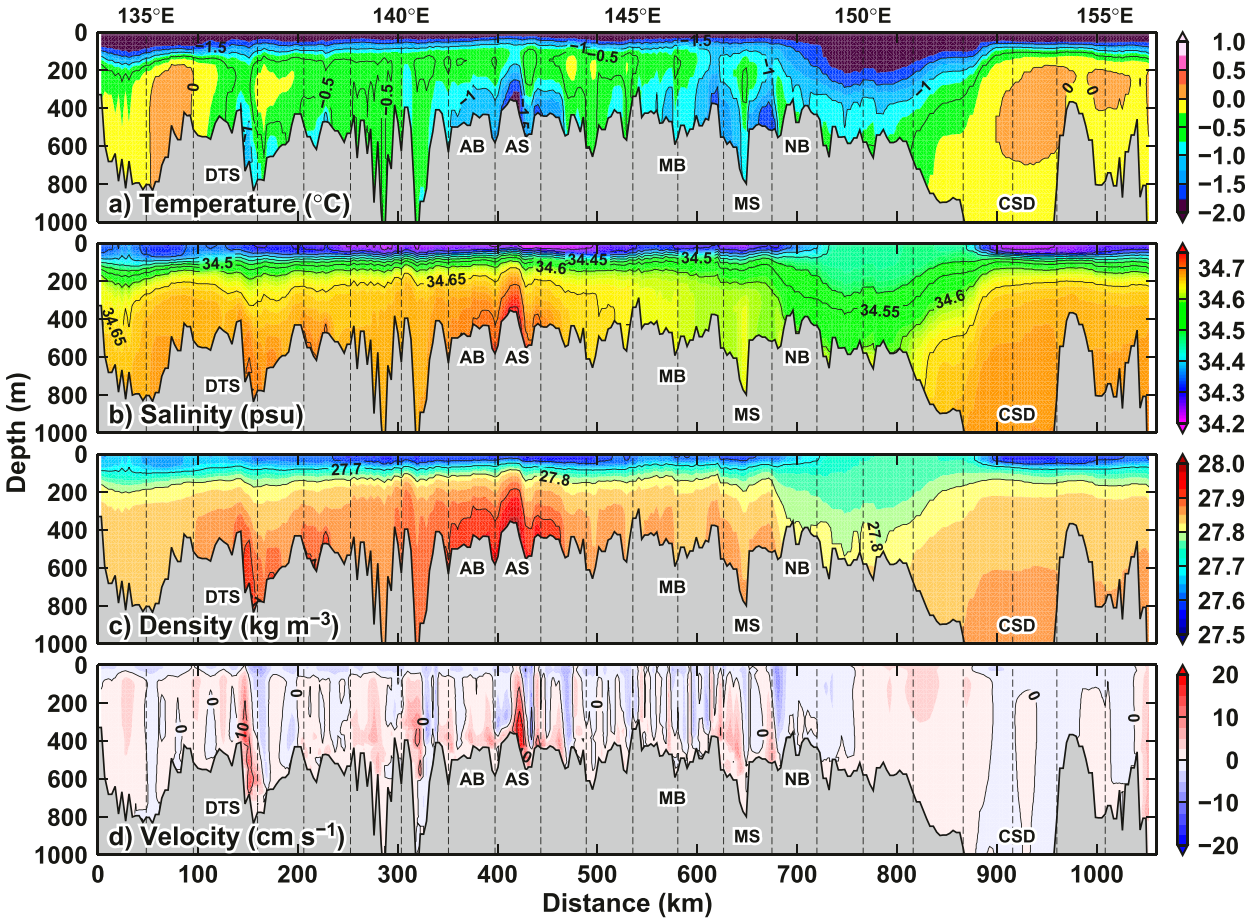

FIG. 9. Vertical sections of (a) potential temperature (°C), (b) salinity (psu), (c) potential density (kg m^{-3}), and (d) the velocity normal to the section (cm s^{-1}) in September along the shelf break between 134° and 156°E in the CTRL case (precalving configuration). Positive (negative) velocity indicates offshore (onshore) advection. The horizontal axis indicates the distance from the western edge (135°E) of the purple line in Fig. 2. DTS stands for the D'Urville Trough Sill. The averaging period is 1979–2013. The other abbreviations are as in Fig. 2.

monthly melt amount from November in the previous year to October in the current year, taking account of seasonal variations (Fig. 5). The magnitude of basal melt in the early 1980s (i.e., 1980–83) is lower than the mean level (17 Gt yr^{-1}), and subsequently the total annual melt varies between 15 and 20 Gt yr^{-1} (Fig. 16).

Coastal easterly winds drive westward flowing ocean currents over the continental slope. Correlation analyses against atmospheric variables (wind, air temperature, and surface air pressure) in the period from 1985 to 2013 (Fig. 17) suggest that the stronger easterly coastal winds enhance the westward flowing coastal current and intrusions of mCDW across the shelf break onto the continental shelf, thus increasing basal melt rates under the MGT (shown as negative correlations near the red box in Fig. 17). Atmospheric variability averaged over the summer (from December to March) is used for the calculations, because basal melting of the MGT is most active in summer. A significant circumpolar negative correlation between MGT basal melting and eastward wind is found in the latitudinal band between 65° and 50°S, and the spatial pattern of surface air pressure is consistent with the negative phase of the southern annular mode (SAM). In fact, after 1985 there is a significant negative correlation (−0.50) between the MGT basal melting and a SAM index (NOAA/National Weather Service/Climate Prediction Center; ftp://ftp.cpc.ncep.noaa.gov/cwlinks/norm.daily.aao.index.b790101.current.ascii). Prior to 1984, there seems to be a positive relationship between the two (Fig. 16).

As discussed in section 3b, the main heat source for the basal melt of the MGT is intrusion of warm mCDW into the shelf region. A vertical profile of the correlation of MGT basal melting with mean ocean temperature averaged from December to March along the southwestern flank of the Mertz Bank is shown in Fig. 18. A significant positive correlation is found in the subsurface layer from 50 to 300 m near the MGT edge (the southern

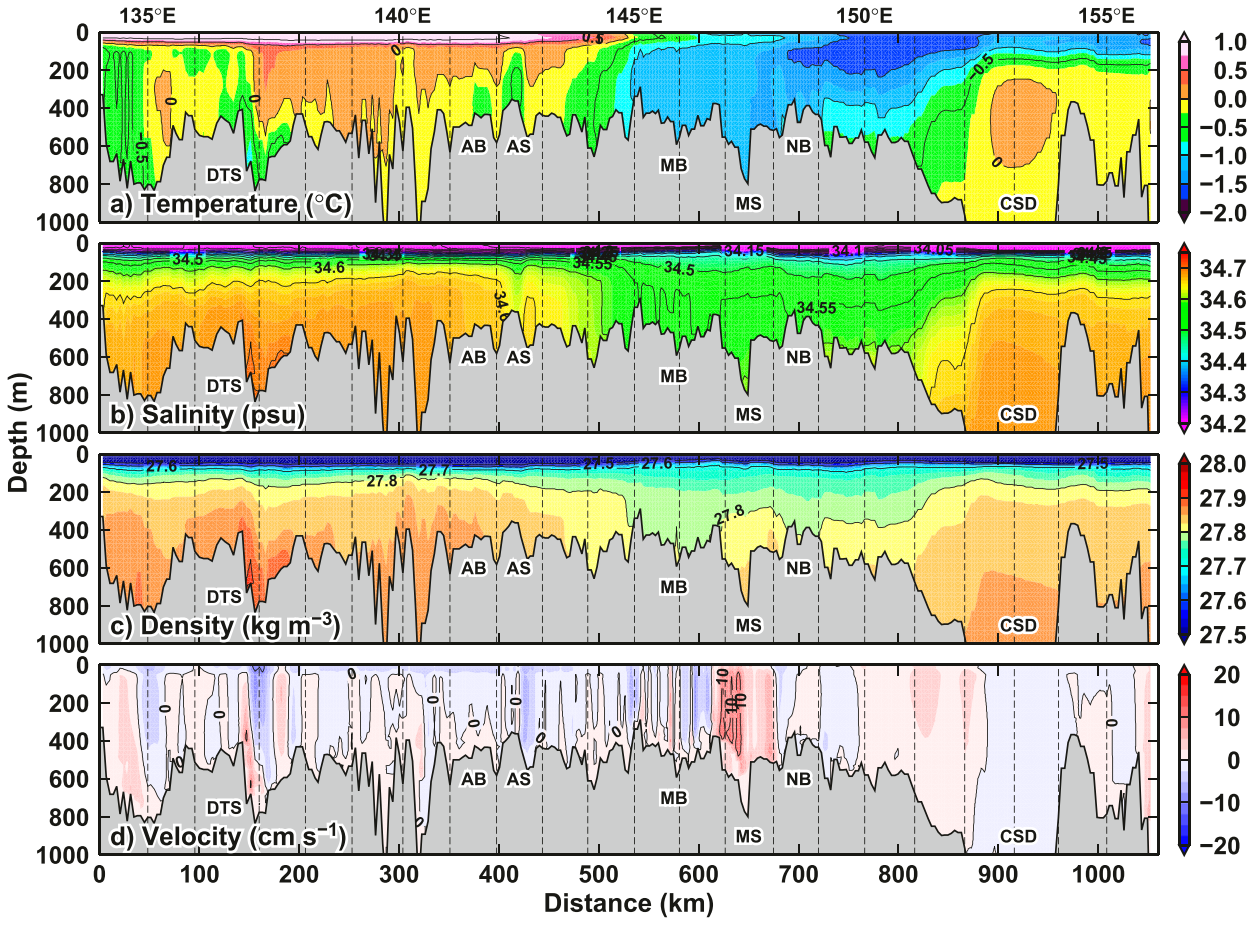

FIG. 10. As in Fig. 9, but for February.

part of the Adélie Depression), which corresponds to a horizontal temperature gradient on the slope (Fig. 8a). No significant correlation exists in the surface layer, where there is strong stratification in density (as shown in Fig. 8a), suggesting that the surface air temperature (Fig. 17b) does not directly contribute to warm subsurface waters flowing into the MGT cavity.

c. *DSW export and bottom properties over the continental slope/rise*

Here we examine the interannual variability of DSW export across the previously defined shelf break sections A–C (Fig. 19a). Annual DSW export is defined as the sum of monthly DSW export from June in the current year to May in the subsequent year. A potential density of 27.88 kg m^{-3} is used as the lower threshold density of DSW. This density threshold is often used as the criterion for DSW from the AGVL region to ultimately form AABW (Bindoff et al. 2001; Williams and Bindoff 2003; Williams et al. 2010). The export of DSW denser than 27.84 kg m^{-3} is also shown for section C, to capture the outflow of relatively less dense DSW from the Mertz Sill.

The interannual variation of DSW export from the three sections concurs with that of local sea ice production (green line in Fig. 19). Similar to the long-term variability of regional sea ice production (Fig. 14), the DSW export shows a decrease from 1979 to the early 1990s, and then a subsequent increase. The DSW exported from sections A, B, and C is significantly correlated with the regional sea ice production, confirming that brine rejection from coastal polynyas drives the variability in the DSW exports.

The variability in DSW export is not related to that in basal melting from the ice shelves and fast ice. From the ocean perspective, active sea ice formation means removing a large amount of freshwater, resulting in salinification (e.g., brine rejection). The effects of sea ice formation and basal meltwater input on ocean density are opposing. A comparison of surface freshwater fluxes caused by sea ice production and the basal melting reveals that the contribution of sea ice production is about

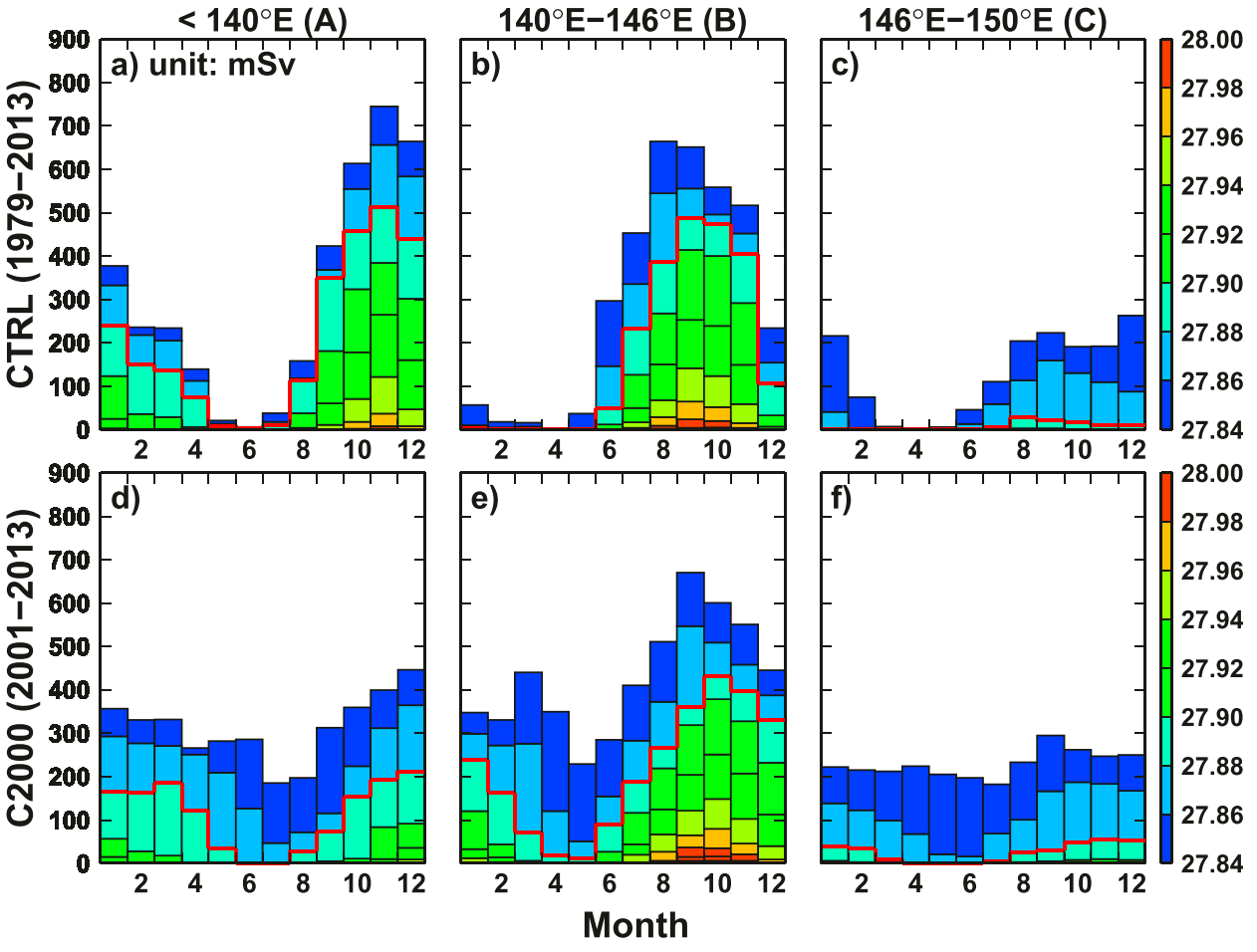

FIG. 11. Seasonal variation of DSW export across the shelf break sections A–C (see purple line in Fig. 2) in the (top) CTRL and (bottom) C2000 cases. The averaging period is 1979–2013 for the CTRL case and 2001–13 for the C2000 case. DSW is defined by water masses which are denser than the potential density of 27.84 kg m^{-3} and cooler than −0.5°C. The color shows the potential density anomaly of the DSW in 0.02 kg m^{-3} bins and the red line indicates 27.88 kg m^{-3}.

one order of magnitude larger than that of basal melting (Figs. 14 and 16). This indicates that sea ice production is the main control on the interannual variation of DSW export from the AGVL region. Through the DSW export, the bottom temperature over the continental slope and rise also fluctuates consistently with the interannual variation of sea ice production (Fig. 19b).

5. Regime shift due to MGT calving

The relocation of iceberg B9B in January–February 2010 dramatically changed the local icescape in the AGVL region; part of the floating ice tongue of the Mertz Glacier (about 75 km in length) calved and most of the thick fast ice on the eastern side of the MGT broke out (Legresy et al. 2010; Massom et al. 2010). Here, we examine the impact of the calving event on the physical environment, based on a comparison of model results in the CTRL and C2000/C2010 cases.

a. Sea ice production

High sea ice production areas on the western side of the MGT and B9B disappear in the C2000 and C2010 cases, but new production areas are formed along the new icescape across the coast between 141° and 151°E (Fig. 3b for the C2010 case). The total sea ice production in the AGVL region averaged from 2010 to 2013 decreased by 26% from 434 to 319 km^3. The change of sea ice production due to the calving event is larger than the interannual variability (standard deviation in the CTRL case: 36 km^3 for 1979–2013), indicating a pronounced change in the surface salt and freshwater balance in the AGVL region. There is no pronounced difference between the C2000 and C2010 cases after 2010 (Fig. 14), confirming that the

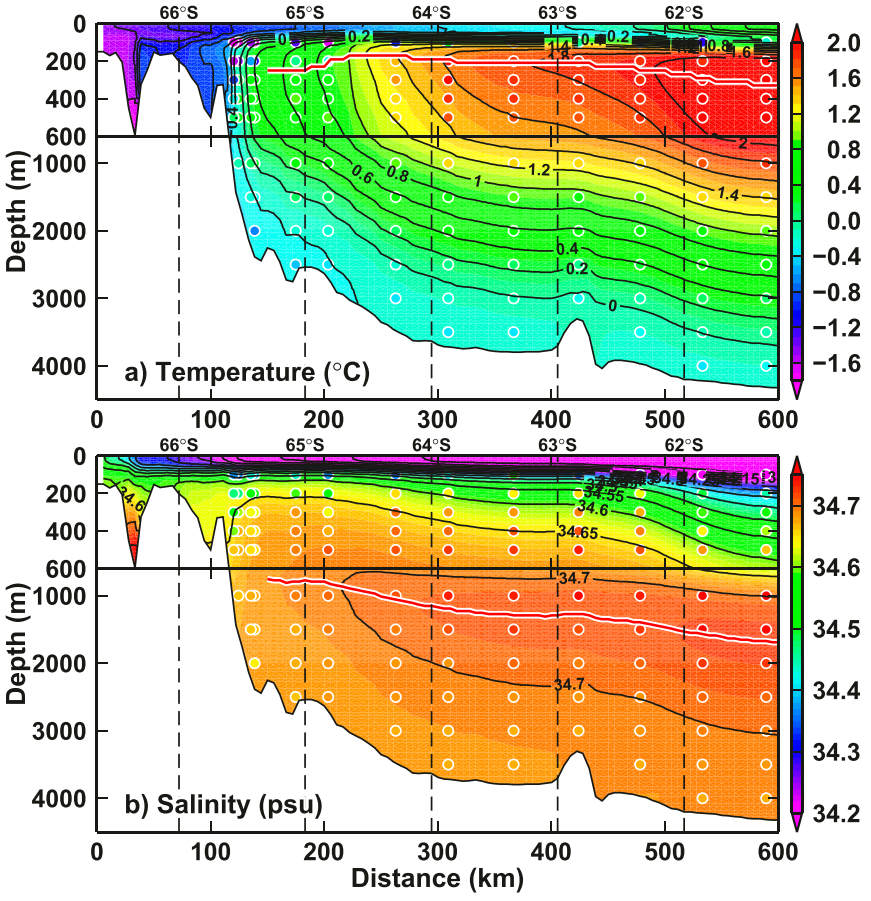

FIG. 12. Vertical section of annual-mean (a) potential temperature and (b) salinity along 140°E in the CTRL case. The annual mean fields are the average over 1979–2013 in the CTRL case. The vertical scale is different above and below 600 m. Red lines indicate the depths of the modeled maximum temperature and salinity in the intermediate depth. Colored circles indicate observed properties in January 1994 (Aoki et al. 2005).

distribution of sea ice production and its total responds quickly to the change in icescape.

b. *Basal melting of ice shelves and fast ice*

The icescape change also resulted in a pronounced decrease in the amount and rate of basal melting from ice shelves and fast ice (Figs. 4b and 16). The total basal melt amount of the MGT decreased substantially from 17.0 to 3.1 Gt yr^{-1}. While the areal extent of the MGT decreased by 40%, the total amount of melt decreased by 70%. The mean melt rate in the southern part of the MGT (A′ in Fig. 4b) substantially decreased from 2.63 to 0.95 m yr^{-1} after the calving event. Mean melt rates of the other ice shelves and fast ice were also reduced.

The change in the temperature profile of water masses flowing into the MGT cavity explains the sharp decrease in the basal melt rate for the regions that remained after calving (Fig. 5). Ocean circulation was dramatically altered by the MGT calving (Fig. 7b). Cold waters are now present in the southern part of the Mertz and Adélie Depressions (i.e., along the coastline or ice front) because new coastal polynyas in the postcalving icescape are now formed there (Fig. 3b). The dominance of cold water in the MGT cavity, which comes from a change of ocean circulation, results in the decreased melt rate of the MGT, ice shelves, and fast ice in the AGVL region.

c. *DSW and AABW*

The icescape change has two different effects on DSW formation in the AGVL. One is that the change in coastal polynya configuration leads to a change in sea ice production distribution and amount, resulting in a large change to the surface salt flux (Fig. 3). The reduction in sea ice production directly leads to a decrease in the formation and export rate of denser classes of DSW in winter (Fig. 11). The other effect is that the change in

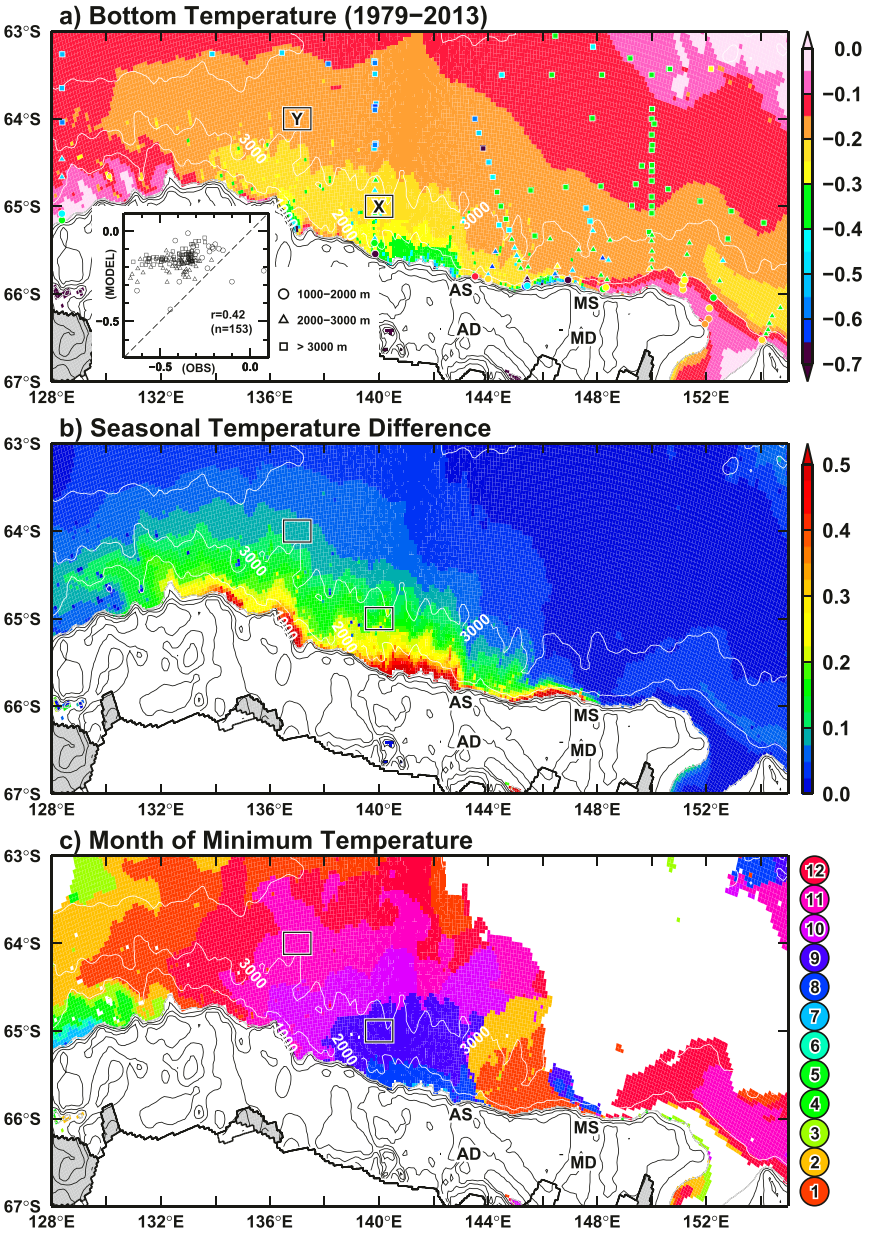

FIG. 13. Horizontal distributions of (a) annual mean bottom temperature, (b) the seasonal temperature difference, and (c) the month that shows the minimum temperature. These plots are based on the annual/monthly mean fields averaged over 1979–2013. In (a), observed temperatures derived from the World Ocean Database 2009 (Boyer et al. 2009) are superimposed as colored symbols. The inset in (a) is a scatterplot of bottom temperature between observation and model. Circles, triangles, and squares show bottom temperature at the regions where the bottom depths are 1000–2000 m, 2000–3000 m, and deeper than 3000 m, respectively. The 95% confidence level for $n = 153$ is at $r = 0.16$. In all panels, the distributions in the region deeper than 1000 m are plotted. Black boxes labeled X and Y show areas used for the comparison of bottom water properties in Fig. 19.

open water area (i.e., the complete removal of the front of the MGT, the large icebergs, and extensive fast ice) leads to substantial modifications to the coastal ocean circulation, resulting in enhanced intrusions of mCDW from east of 150°E onto the continental shelf. The increase in mCDW means an increase of warmer and less saline waters relative to cold and saline waters originating from coastal sea ice production, eventually

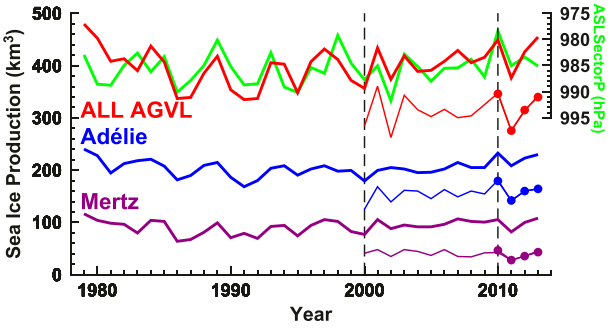

FIG. 14. Time series of modeled annual mean sea ice production in the AGVL region. Blue, purple, and red lines indicate sea ice production over the Adélie Depression, the Mertz Depression, and the whole of the AGVL region, respectively (see areas enclosed by gray lines in Fig. 3). The green line shows the time series of mean sea level pressure in the Amundsen and Bellingshausen Seas (Hosking et al. 2013; https://legacy.bas.ac.uk/data/absl/, the variable name: ASLSectorP), averaged over winter (May–October). Vertical dashed lines indicate the start of the postcalving experiments (C2000 and C2010 cases). Thin lines without and with dots indicate results from the C2000 and C2010 cases, respectively.

leading to an increase in lighter DSW export in spring and summer (Fig. 11). At the three shelf break sections (the Adélie Sill/Bank, the Mertz Sill/Bank, and the D'Urville Trough Sill), the combination of these two effects changes the DSW export and subsequent water properties over the continental slope and rise.

The calving event has extensive effects on the bottom properties over the AGVL continental shelf, slope, and rise (Fig. 20). The anomalies in temperature and salinity are calculated by subtracting the annual mean fields for 2001–13 in the CTRL case from those in the C2000 case. Different color scales are used for the continental shelf and continental slope/rise regions, because the magnitude of the anomaly is significantly different in the two regions across the shelf break. Enhanced signals of mCDW (warming and increased salinity) are found over the Ninnis Bank and the Mertz Depression. This signal in the annual mean field extends to the Adélie Depression. These salinification signals over the continental shelf result from enhanced intrusions of mCDW from the Cook Shelf Depression. Even though the surface salt flux over the Adélie Depression is reduced (Fig. 3), the bottom salinity in the annual mean field is increased with the salinity compensation by the enhanced mCDW intrusion. Note that the reduction in sea ice production leads to a decrease of DSW export from the Adélie Sill/Bank and the winter salinity in the Adélie Depression. An extensive freshening signal over the continental shelf west of 142°E results from the reduction in surface salt flux over the Adélie Depression.

In the CTRL case, dense and cold water predominantly occupies the Mertz Depression, and a strong west–east density front is formed between 150° and

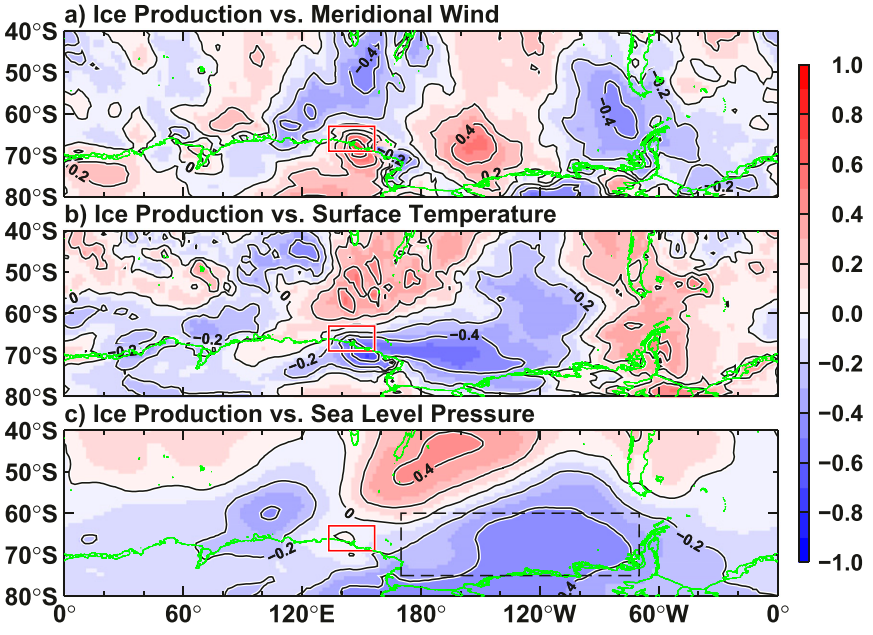

FIG. 15. Correlation maps of modeled sea ice production in the AGVL region with atmospheric surface variables (a) meridional wind, (b) surface temperature, and (c) sea level pressure for the period 1979–2013. The red box shows the AGVL region. In (c), the dashed line shows the defined areas for calculation of the variable ASLSectorP in Hosking et al. (2013). The 95% confidence level (1979–2013, $n = 36$) is at $r = 0.33$.

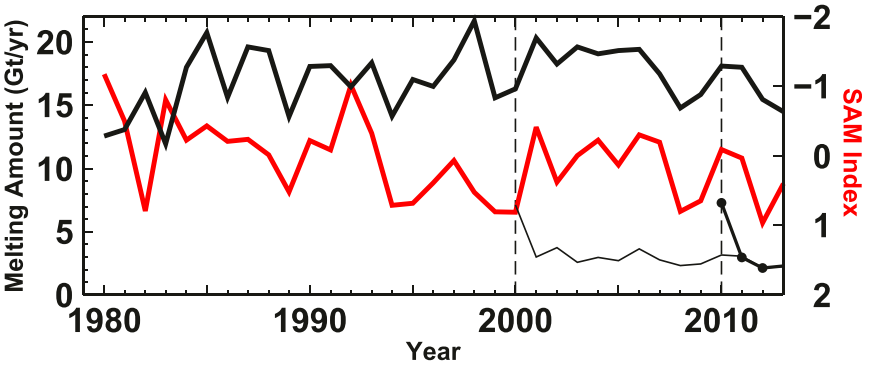

FIG. 16. Time series of total annual basal melt under the MGT (black) and the SAM index (red). Thin lines without and with dots indicate results from the C2000 and C2010 cases, respectively. Vertical dashed lines indicate the start of the postcalving experiments (C2000 and C2010 cases). The mass exchange between ice shelf and ocean is expressed as $\rho_i w_i$ or $\rho_o w_o$, where ρ and w are density and vertical velocity, respectively, and the subscripts of i and o indicate ice shelf and ocean, respectively. The basal melting amount is calculated from $\rho_o w_o$ with the seawater density of 1028 kg m^{-3}.

152°E (Fig. 21). Warm water from the Cook Shelf Depression is redirected northward by the density front nearly aligned with the topographic contour. In the C2000 case, the density front is not formed because of the reduction of coastal sea ice production (Fig. 3b). There is a rather weak south–north density gradient, which enables warm mCDW to intrude westward onto the continental shelf region.

Next, we show the influence of the calving event on the DSW export. DSW transport, with a 0.02 kg m^{-3} bin interval of potential density, is estimated to avoid dependence on the selected threshold. The influence on DSW export is assessed from the profile of cumulative DSW export (Fig. 22). The net reduction of sea ice production over the AGVL region leads to reduction in denser DSW export, and enhanced mCDW transport from the east leads to an increase in lighter DSW export (Fig. 22d). The change in DSW export depends on the export region.

In section A (the D'Urville Trough Sill), export of DSW denser than 27.86 kg m^{-3} is substantially decreased due to the reduction in sea ice production over the Adélie Depression. In section B (the Adélie Sill/Bank), export

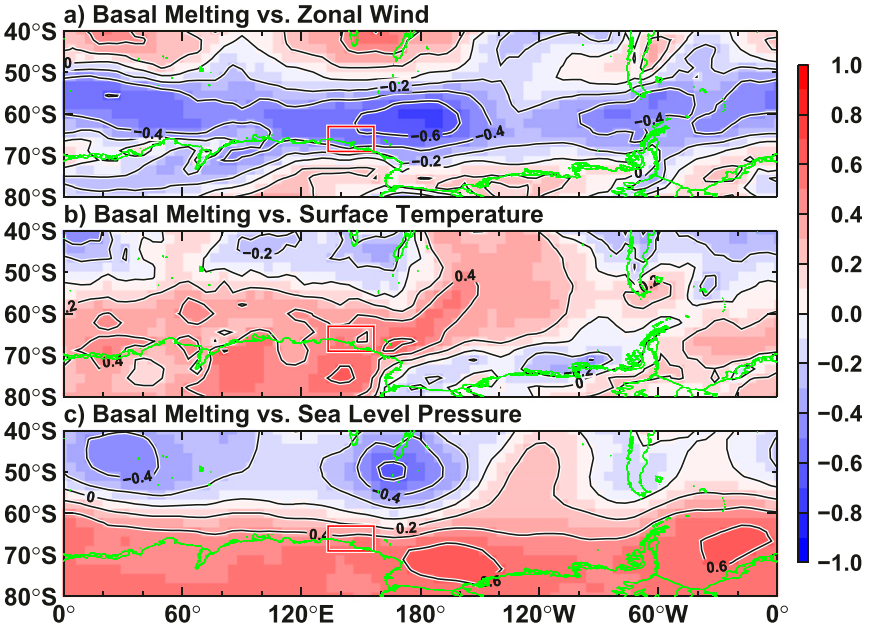

FIG. 17. Correlation maps of basal melt beneath the MGT with atmospheric surface variables (a) eastward wind, (b) surface temperature, and (c) sea level pressure for the period 1985–2013. The red box shows the AGVL region. The 95% significant level (1985–2013, $n = 29$) is at $r = 0.37$.

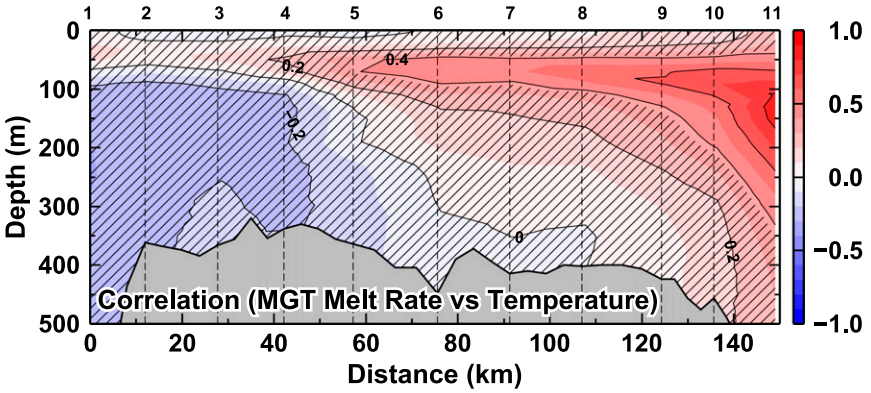

FIG. 18. Vertical profiles of the correlation between ocean temperature and basal melt at the MGT for the period 1985–2013. Unshaded areas exceed the 95% significance level ($r = 0.37$). Numbers on the upper horizontal axis indicate positions along the southwestern flank of the Mertz Bank (see Fig. 7).

of DSW denser than 27.90 kg m^{-3} slightly decreases, but that of DSW lighter than 27.88 kg m^{-3} increases, resulting from a combination of changes in surface salt flux and mCDW on the shelf region. In section C (the Mertz Sill/Bank), enhanced mCDW increases the total DSW export. A reduction in denser DSW export occurs in winter and an increase in lighter DSW export is observed in spring and summer (Fig. 11).

Cooling/freshening and warming/salinification signals are also found over the continental slope and rise regions west and east of 143°E, respectively (Fig. 20). The freshening signals are just offshore from the shelf break in sections A and B, where the export of denser DSW is decreased by the reduction of sea ice production in the AGVL region. The cooling signal results from the increase in lighter DSW export. The warming/salinification

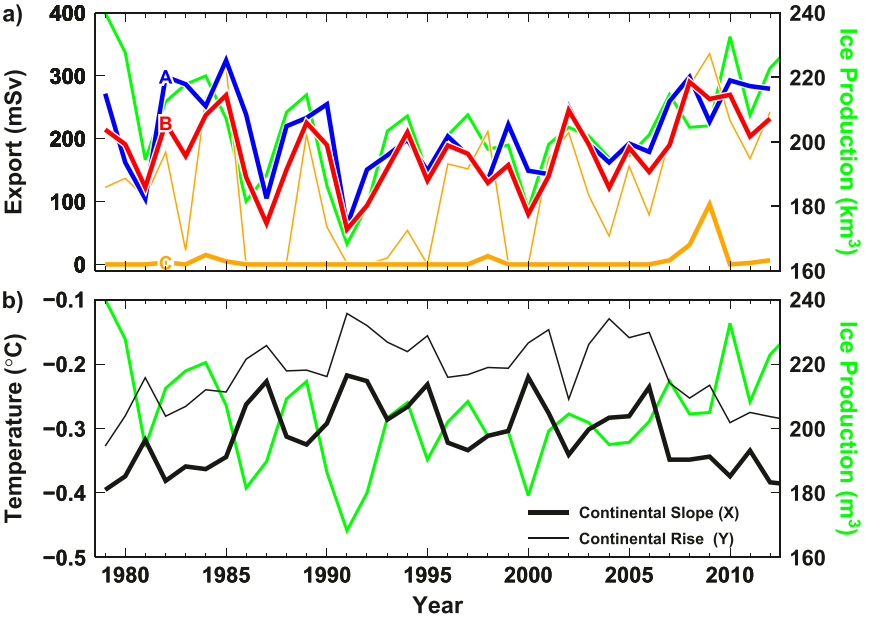

FIG. 19. Time series of (a) DSW export and (b) bottom temperature on the continental slope and rise (see boxes labeled by X and Y in Fig. 13 for the locations). Thick blue, red, and orange lines indicate export of DSW denser than 27.88 kg m^{-3}, from sections A, B, and C, respectively. The thin orange line indicates export of DSW denser than 27.84 kg m^{-3} from section C. The green line indicates the interannual variability of modeled sea ice production over the Adélie Depression, as a representative of the AGVL region. The black thick and thin lines in (b) correspond to the bottom temperature on continental slope and rise, respectively.

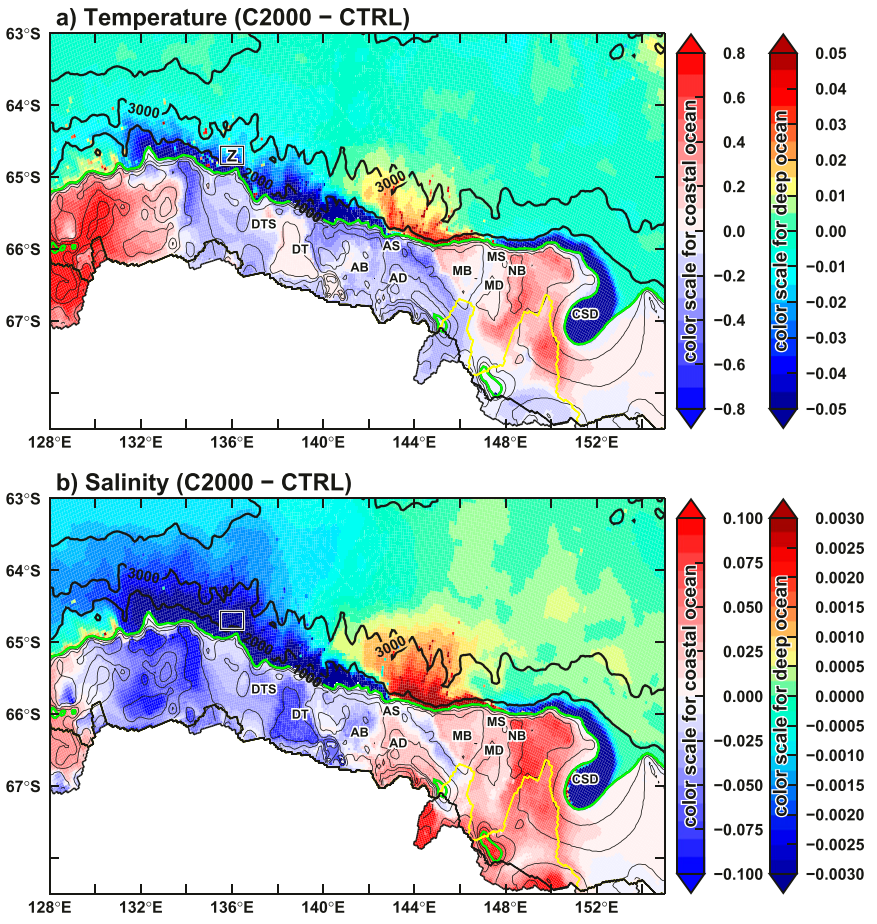

FIG. 20. Map of differences in annual mean bottom water properties, that is, (a) temperature and (b) salinity between the C2000 and CTRL cases (C2000 − CTRL). The annual mean fields are calculated for the period 2001–13. The green lines are the 1000-m depth contour (i.e., the approximate position of the shelf break). Color scales are different in the continental shelf and deep ocean regions. The box labeled with Z indicates an area used in Fig. 23. Location names are as in Fig. 2.

signals are offshore from the Mertz Bank, corresponding to the pathway of DSW from the Mertz Depression. In the Mertz Depression, warmer and more saline mCDW comes from the east and enhances the mCDW contribution to local dense water formation, resulting in a warming and salinification of the bottom water properties over the continental slope and rise.

Finally, the change in bottom properties is quantitatively compared with the seasonal and interannual variability to assess the impact of the calving event (Fig. 23). We select an area over the continental slope around 136°E (see the box marked "Z" in Fig. 20), where the change in bottom properties is relatively large. The effect of the modeled calving event is to reduce the mean bottom temperature, averaged over the period 2001–13, by 0.031°C and the mean salinity by 0.0046 psu. The change in bottom temperature caused by the calving event is smaller than the seasonal and interannual variability. However, the bottom salinity change has a comparable magnitude to the interannual variability, indicating that the MGT calving has an impact on the salinity over the continental slope and rise regions. Note that the results in the C2010 case show similar changes to the C2000 case, for the period of overlap (2010–13).

6. Summary and discussion

We investigated the annual, seasonal, and interannual variabilities in sea ice, ice shelves/fast ice basal melting, and the ocean properties around the AGVL region, East Antarctica, and examined the responses of each to the icescape change resulting from the MGT calving event. The modeled sea ice production and its spatial pattern (Fig. 3) are consistent with the satellite-based estimates

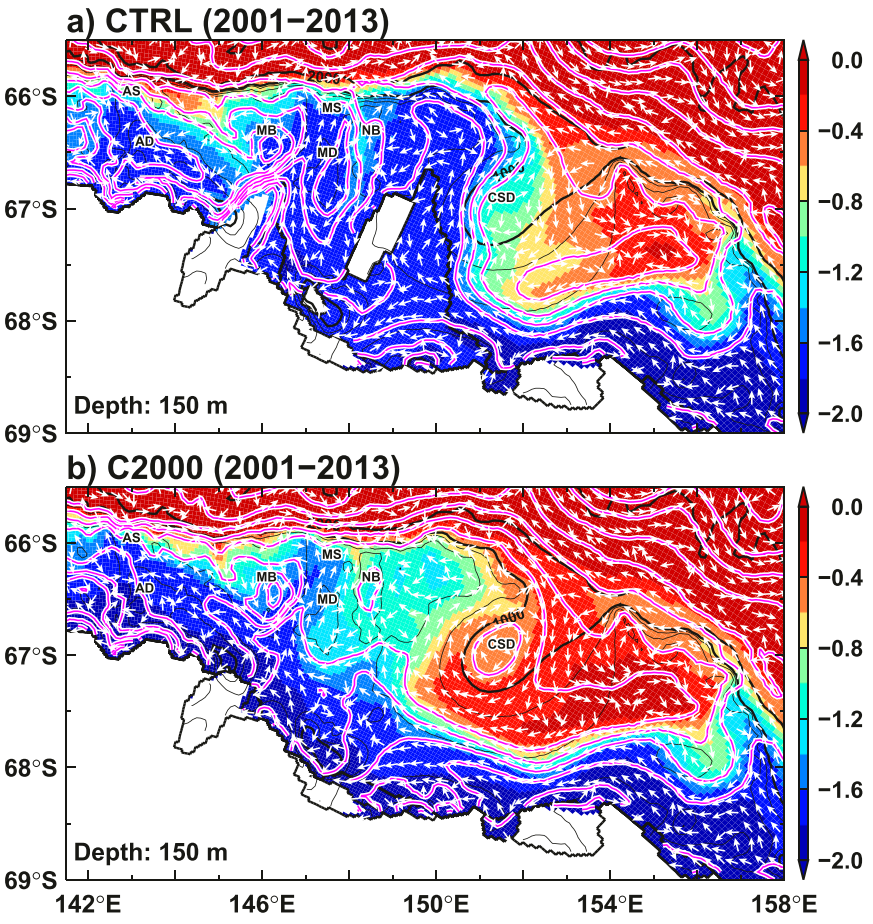

FIG. 21. Map of annual mean temperature (colored), potential density (pink contour), and ocean flow direction at 150-m depth. The annual mean in this figure is for 2001–13. Location names are as in Fig. 2.

of Tamura et al. (2008), as well as previous ocean–sea ice modeling studies (Marsland et al. 2004; Kusahara et al. 2010, 2011a). In the region between 140° and 149°E, active sea ice production areas where the annual production is higher than 10 m yr^{-1} are reproduced along the coastline or the edges of ice shelves, icebergs, and fast ice.

The regional sea ice production in the model is significantly correlated with the local offshore wind and colder air temperature on interannual time scales (Fig. 15). Sea ice production has a significant correlation with sea level pressure variability over the Amundsen–Bellingshausen Seas (Fig. 14). With the AGVL region located on the western part of the pressure system and this result that the AGVL regional atmospheric variabilities are coupled with the pressure system, it is therefore intuitive that cold offshore winds from the Antarctic continent enhance the local sea ice production in the AGVL region.

The MGT calving significantly changed the icescape in the AGVL region, resulting in large changes to sea ice production, in terms of both its amount and distribution (Fig. 3). The total sea ice production after the calving event is reduced by approximately 26%, which is larger than the range of interannual variability, indicating that the calving event strongly impacts sea ice and ocean (Fig. 14). This magnitude of the reduction in regional sea ice production roughly coincides with the satellite estimate of 14%–20% by Tamura et al. (2012).

We have estimated the basal melt amount and rate of ice shelves, large icebergs, and fast ice in the model (Fig. 4 and Table 2). The basal melt of these elements is high in summer and low in winter (Figs. 5 and 6). The large interannual summer variability is controlled by the magnitude of warm water intrusion from the shelf break (Figs. 7, 8, and 18). In contrast, the winter melt amount and rate are very stable because of the dominance of waters at the surface freezing point temperatures in the MGT cavity (Fig. 5).

The annual mean melt rate of the MGT in the pre-calving configuration is 3.1 m yr^{-1} and the total melt amount is 17.0 Gt yr^{-1}, which is larger than recent

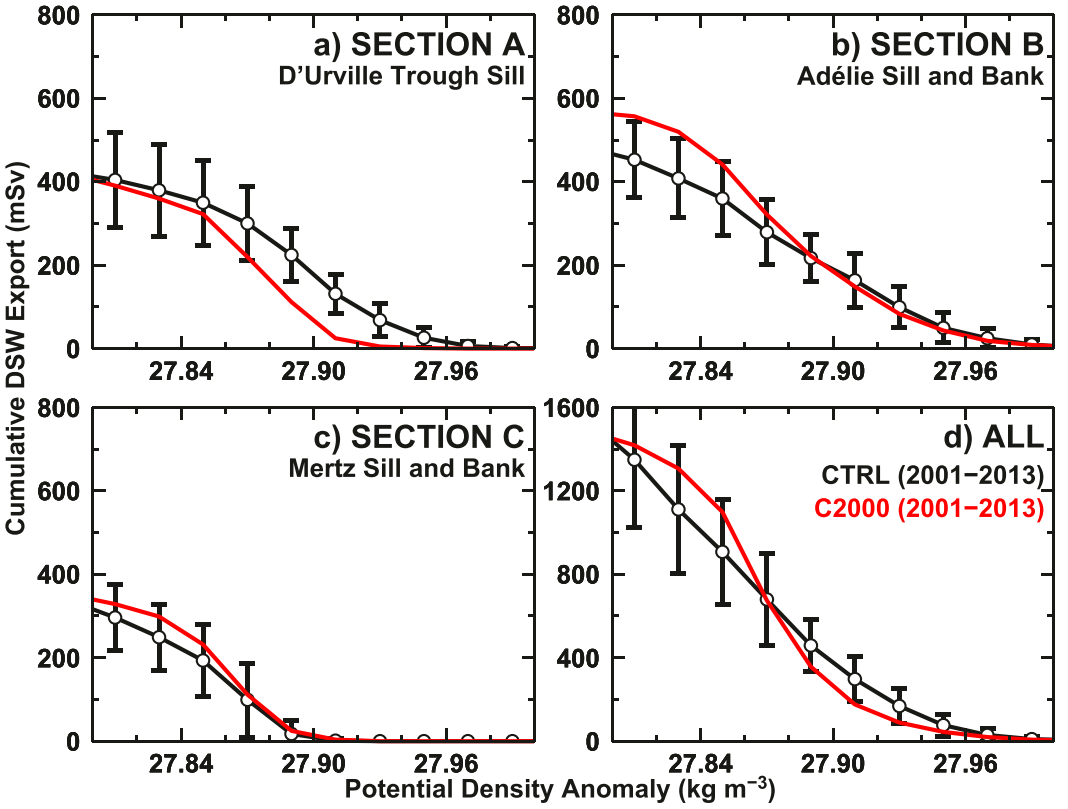

FIG. 22. Cumulative DSW export from the AGVL region. Black and red lines show the CTRL and C2000 cases, respectively. The standard deviation (i.e., the interannual variability) is shown for the CTRL case only.

observational and modeling studies (Table 3). It is found that the basal melt of fast ice contributes approximately 25% to the regional meltwater flux (Table 2). Areas of highest basal melt areas are present on the northwestern/western side of ice shelves, large icebergs, and fast ice, where warm waters intrude from the continental slope (Figs. 6, 5c, 7, and 8). Correlation analyses between the MGT basal melting and surface atmospheric variables reveal that the strong westward coastal wind enhances the intrusion of warm water onto the continental shelf (Figs. 17 and 18) and leads to high basal melt of the MGT. The icescape change associated with the MGT calving event substantially modifies the pattern of water masses flowing into the MGT cavity, from warm waters to near-surface freezing temperature waters (Fig. 5). The change in water masses results in a lower mean basal melt rate (Fig. 4 and Table 2).

DSW over the AGVL continental shelf outflows through three regions: the Adélie and Mertz Sills/Banks and the D'Urville Trough Sill (Figs. 9, 10, 11, and 13). Our modeling result suggests a triple system for DSW export. The characteristics of the DSW exported from the Adélie and Mertz Sills/Banks agree with previous observational and modeling studies (Williams et al. 2010; Kusahara et al. 2011a). At the moment, there are no direct observations available to validate the DSW export from the D'Urville Trough Sill; however, some studies of sedimentation have speculated on the existence of a DSW outflow here (Denis et al. 2006; Crosta et al. 2008; Presti et al. 2011). DSW exports from the Adélie and Mertz Sills/Banks peak in winter (Fig. 11), consistent with a seasonal variation in sea ice production in the AGVL region. In contrast, the peak month of DSW export from the D'Urville Trough Sill is delayed by two months. Given that there is no pronounced sea ice production over the D'Urville Trough, DSW export from the D'Urville Trough Sill is controlled remotely by the sea ice production in the Adélie Depression, with a time lag of two months corresponding to an advection time of high-salinity water from the east. The interannual variability of DSW export from the three sills is related to local sea ice production in the AGVL region (Figs. 14 and 19). The contribution of sea ice production to the freshwater balance is about one order of magnitude larger than that of the basal melting of ice shelves and fast ice, in terms of the mean and its variability (Figs. 14 and 16). This confirms that sea ice production is the main factor in DSW formation and variation.

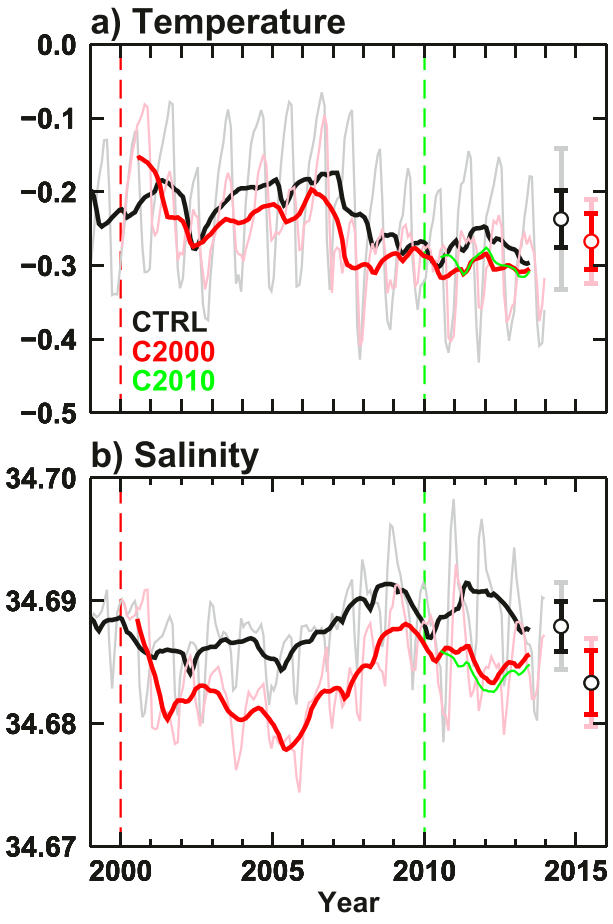

FIG. 23. Time series of bottom properties (a) temperature and (b) salinity on the continental slope (within the box labeled with Z in Fig. 20). Light lines show monthly averaged values and dark lines show the 13-month running averages. Mean values and standard deviations for the CTRL and C2000 cases are shown on the right. Vertical red and green dashed lines indicate the start of the postcalving experiments (the C2000 and C2010 cases).

The change in the regional icescape due to the MGT calving has two effects on DSW export: a reduction in the export of the denser DSW from a reduction in sea ice production (Fig. 3) and an increase in the export of lighter DSW from enhanced mCDW intrusions onto continental shelf regions (Figs. 11, 20, and 21). The responses of the DSW export from the three regions are different (Fig. 22). From the Mertz Sill/Bank, an increase of mCDW inflow slightly enhances the export of lighter DSW. From the Adélie Sill/Bank, on the other hand denser DSW export decreases and lighter DSW increases. From the D'Urville Trough Sill, the reduction in sea ice production over the Adélie Depression results in a decrease of DSW export. The changes to DSW export lead to consistent changes in bottom water properties over the continental slope and rise regions (Figs. 20 and 23). Strong freshening signals are found off the Adélie Sill/Bank and D'Urville Trough Sill, and warming/salinification is produced off the Mertz Sill/Bank.

In our previous study (Kusahara et al. 2011b), we used a coupled ocean–sea ice model, in which ice shelves, large icebergs, and fast ice were fixed as land points and there was no ocean–ice shelf interaction. Our present study results are consistent with the previous one, in terms of the total reduction of sea ice production and denser DSW export caused by the MGT calving. However, in the previous model, there was a large reduction in denser DSW export from the Mertz Depression, inconsistent with this study. Since the Mertz Depression was semiclosed by solid land grid points in the previous model, the DSW in the depression before the calving event had a higher density than that in the present model.

There are some limitations in the present study, as identified by comparing the model with observations. We have discussed the impacts of the MGT calving event, based on the two extreme pre- and postcalving configurations. However, the actual icescape in the AGVL region changes with time, and time-varying changes in the position of B9B position and the fast ice distribution would be crucial for the distribution of the surface salinity, freshwater, and momentum fluxes (Tamura et al. 2016). In situ ocean observations reported pronounced freshening signals of DSW in the Adélie Depression following the calving (Shadwick et al. 2013; Lacarra et al. 2014). Contrary to the observed freshening, our model showed that, in the postcalving configuration, the reduction in the surface salinity flux is compensated by lateral salinity flux by enhanced mCDW intrusions from the east (Fig. 21). The difference may arise from our model limitation of time-independent configurations (i.e., only the two extreme configurations).

Our model does realistically reproduce the vertical profile of water masses along 140°E (Fig. 12) and the bottom temperature distribution off the AGVL region. However, there are warm biases in the bottom temperature (Figs. 12a and 13a), which are likely related to the insufficient horizontal and vertical resolution in the model. While the model has fine horizontal resolution in the AGVL region, the horizontal resolution in the other DSW and AABW formation regions (e.g., the Ross Sea; ~15 km) is not sufficient to represent circumpolar dense water formation and outflow processes. Observations have shown that Ross Sea Bottom Water plays an important role in bottom water properties in the Australian Antarctic basin (Jacobs and Giulivi 2010; Shimada et al. 2012), and thus poor representation of the remote

bottom water formation would also result in warm biases in the bottom temperatures. We adopted z coordinates for the vertical coordinate system, but it is known that very high resolution is required to adequately represent downslope flow of dense waters (Wang et al. 2008). Although we used a relatively high vertical resolution of 20–50 m, this may be still insufficient for reproducing downslope processes and it also leads to excessive mixing with warm water and subsequent warm biases at bottom. Related to this problem, the excessive mixing may lead to a weak response of bottom properties to the MGT calving event.

Numerical experiments before and after the MGT calving event reveal that icescape changes have wide impacts on interconnected physical systems all over the AGVL region (i.e., sea ice production, basal melt of ice shelves and fast ice, DSW formation and export on the continental shelf, and AABW over the continental slope and rise). A recent study by Campagne et al. (2015) has suggested, from analysis of sediment core data, that the Mertz Polynya activity is regulated not only by atmospheric variability on interannual time scales but also by such calving events on centennial time scales.

Our modeling study suggests that regional icescape changes have wide-ranging impacts on physical systems through changes to sea ice production and ocean circulation that are themselves connected. This indicates that changing the Antarctic coastal configuration with a scale of several tens of kilometers can extensively change the basin-scale Southern Ocean and Antarctic cryosphere. Generally, changes to the Antarctic ice shelves occur regularly. Rapid increases of ice discharge from the Antarctic Ice Sheet over the past few decades are being reported from satellite observations (Rignot et al. 2008), indicating the possibility of further icescape changes in the near future. This strongly underlines the need to monitor ice shelves, sea ice, and fast ice, which are linked by ocean processes. Needless to say, further improvement of numerical models, for example dynamic fast ice (Lemieux et al. 2015), is required to better simulate and understand coastal processes in time-dependent configurations (Tamura et al. 2016). Combinations of in situ and satellite observations with improvements in numerical modeling are very important for assessing the changing nature of the Southern Ocean and Antarctic climate systems.

Acknowledgments. This research was supported by the Australian Government's Antarctic Cooperative Research Centre Programme through the ACE CRC, the Canon Foundation, and the Grant for Joint Research Program of the Institute of Low Temperature Science, Hokkaido University. It contributes to AAS Project 4116 and the World Climate Research Programme (WCRP) Climate and Cryosphere Project (CliC) project Targeted Activity "Interactions between Cryospheric Elements." KK was supported by Research Activity Start-up 25887001 from the Japan Society for the Promotion of Science (JSPS). HH was supported by JSPS KAKENHI Grant 26247080. AF was supported by JSPS KAKENHI Research Project 13F03748. SA was supported by JSPS KAKENHI Grant 25281001. GW was supported by the Australian Research Council's Future Fellowship program. TT was supported by JSPS KAKENHI Grant 26740007. Numerical calculations were performed on FX10 at Information Technology Center, the University of Tokyo. We are grateful to Dr. Laurence Padman and an anonymous reviewer for constructive comments on the manuscript.

REFERENCES

Adcroft, A., C. Hill, and J. Marshall, 1997: Representation of topography by shaved cells in a height coordinate ocean model. *Mon. Wea. Rev.*, **125**, 2293–2315, doi:10.1175/1520-0493(1997)125<2293:ROTBSC>2.0.CO;2.

Aoki, S., S. R. Rintoul, S. Ushio, S. Watanabe, and N. L. Bindoff, 2005: Freshening of the Adélie Land Bottom Water near 140°E. *Geophys. Res. Lett.*, **32**, L23601, doi:10.1029/2005GL024246.

Barber, D. G., and R. A. Massom, 2007: The role of sea ice in Arctic and Antarctic polynyas. *Polynyas: Windows to the World*, W. O. Smith and D. G. Barber, Eds., Elsevier Oceanography Series, Vol. 74, Elsevier, 1–54, doi:10.1016/S0422-9894(06)74001-6.

Berthier, E., B. Raup, and T. Scambos, 2003: New velocity map and mass-balance estimate of Mertz Glacier, East Antarctica, derived from Landsat sequential imagery. *J. Glaciol.*, **49**, 503–511, doi:10.3189/172756503781830377.

Bindoff, N. L., G. D. Williams, and I. Allison, 2001: Sea-ice growth and water-mass modification in the Mertz Glacier polynya, East Antarctica, during winter. *Ann. Glaciol.*, **33**, 399–406, doi:10.3189/172756401781818185.

Boyer, T. P., and Coauthors, 2009: *World Ocean Database 2009*. S. Levitus, Ed., NOAA Atlas NESDIS 66, 216 pp. [Available online at ftp://ftp.nodc.noaa.gov/pub/WOD09/DOC/wod09_intro.pdf.]

Campagne, P., and Coauthors, 2015: Glacial ice and atmospheric forcing on the Mertz Glacier polynya over the past 250 years. *Nat. Commun.*, **6**, 6642, doi:10.1038/ncomms7642.

Cougnon, E. A., B. K. Galton-Fenzi, A. J. S. Meijers, and B. Legrésy, 2013: Modeling interannual dense shelf water export in the region of the Mertz Glacier tongue (1992–2007). *J. Geophys. Res.*, **118**, 5858–5872, doi:10.1002/2013JC008790.

Crosta, X., D. Denis, and O. Ther, 2008: Sea ice seasonality during the Holocene, Adélie Land, East Antarctica. *Mar. Micropaleontol.*, **66**, 222–232, doi:10.1016/j.marmicro.2007.10.001.

Dee, D. P., and Coauthors, 2011: The ERA-Interim reanalysis: Configuration and performance of the data assimilation system. *Quart. J. Roy. Meteor. Soc.*, **137**, 553–597, doi:10.1002/qj.828.

Denis, D., X. Crosta, S. Zaragosi, O. Romero, B. Martin, and V. Mas, 2006: Seasonal and subseasonal climate changes

recorded in laminated diatom ooze sediments, Adélie Land, East Antarctica. *Holocene*, **16**, 1137–1147, doi:10.1177/0959683606069414.

Depoorter, M. A., J. L. Bamber, J. A. Griggs, J. T. M. Lenaerts, S. R. M. Ligtenberg, M. R. van den Broeke, and G. Moholdt, 2013: Calving fluxes and basal melt rates of Antarctic ice shelves. *Nature*, **502**, 89–92, doi:10.1038/nature12567.

Dinniman, M. S., J. M. Klinck, L.-S. Bai, D. H. Bromwich, K. M. Hines, and D. M. Holland, 2015: The effect of atmospheric forcing resolution on delivery of ocean heat to the Antarctic floating ice shelves. *J. Climate*, **28**, 6067–6085, doi:10.1175/JCLI-D-14-00374.1.

Dragon, A.-C., M.-N. Houssais, C. Herbaut, and J.-B. Charrassin, 2014: A note on the intraseasonal variability in an Antarctic polynia: Prior to and after the Mertz Glacier calving. *J. Mar. Syst.*, **130**, 46–55, doi:10.1016/j.jmarsys.2013.06.006.

Fraser, A. D., R. A. Massom, K. J. Michael, B. K. Galton-Fenzi, and J. L. Lieser, 2012: East Antarctic landfast sea ice distribution and variability, 2000–08. *J. Climate*, **25**, 1137–1156, doi:10.1175/JCLI-D-10-05032.1.

Gent, P. R., J. Willebrand, T. J. McDougall, and J. C. McWilliams, 1995: Parameterizing eddy-induced tracer transports in ocean circulation models. *J. Phys. Oceanogr.*, **25**, 463–474, doi:10.1175/1520-0485(1995)025<0463:PEITTI>2.0.CO;2.

Giles, A. B., R. A. Massom, and V. I. Lytle, 2008: Fast-ice distribution in East Antarctica during 1997 and 1999 determined using RADARSAT data. *J. Geophys. Res.*, **113**, C02S14, doi:10.1029/2007JC004139.

Hellmer, H. H., and D. J. Olbers, 1989: A two-dimensional model for the thermohaline circulation under an ice shelf. *Antarct. Sci.*, **1**, 325–336, doi:10.1017/S0954102089000490.

Hibler, W. D., III, 1979: A dynamic thermodynamic sea ice model. *J. Phys. Oceanogr.*, **9**, 815–846, doi:10.1175/1520-0485(1979)009<0815:ADTSIM>2.0.CO;2.

Holland, D. M., and A. Jenkins, 1999: Modeling thermodynamic ice–ocean interactions at the base of an ice shelf. *J. Phys. Oceanogr.*, **29**, 1787–1800, doi:10.1175/1520-0485(1999)029<1787:MTIOIA>2.0.CO;2.

Hosking, J. S., A. Orr, G. J. Marshall, J. Turner, and T. Phillips, 2013: The influence of the Amundsen–Bellingshausen Seas low on the climate of West Antarctica and its representation in coupled climate model simulations. *J. Climate*, **26**, 6633–6648, doi:10.1175/JCLI-D-12-00813.1.

Hunke, E. C., and J. K. Dukowicz, 1997: An elastic–viscous–plastic model for sea ice dynamics. *J. Phys. Oceanogr.*, **27**, 1849–1867, doi:10.1175/1520-0485(1997)027<1849:AEVPMF>2.0.CO;2.

IOC, IHO, and BODC, 2003: *GEBCO Digital Atlas*. Centenary ed., Intergovernmental Oceanographic Commission, International Hydrographic Organization and British Oceanographic Data Centre, CD-ROM. [Available online at http://www.gebco.net/data_and_products/gebco_digital_atlas/.]

Jacobs, S. S., and C. F. Giulivi, 2010: Large multidecadal salinity trends near the Pacific–Antarctic continental margin. *J. Climate*, **23**, 4508–4524, doi:10.1175/2010JCLI3284.1.

——, H. H. Hellmer, C. S. M. Doake, A. Jenkins, and R. M. Frolich, 1992: Melting of ice shelves and the mass balance of Antarctica. *J. Glaciol.*, **38**, 375–387, doi:10.3198/1992JoG38-130-375-387.

Kara, A. B., P. A. Rochford, and H. E. Hurlburt, 2000: Efficient and accurate bulk parameterizations of air–sea fluxes for use in general circulation models. *J. Atmos. Oceanic Technol.*, **17**, 1421–1438, doi:10.1175/1520-0426(2000)017<1421:EAABPO>2.0.CO;2.

Kern, S., 2009: Wintertime Antarctic coastal polynya area: 1992–2008. *Geophys. Res. Lett.*, **36**, L14501, doi:10.1029/2009GL038062.

Kusahara, K., and H. Hasumi, 2013: Modeling Antarctic ice shelf responses to future climate changes and impacts on the ocean. *J. Geophys. Res.*, **118**, 2454–2475, doi:10.1002/jgrc.20166.

——, and ——, 2014: Pathways of basal meltwater from Antarctic ice shelves: A model study. *J. Geophys. Res.*, **119**, 5690–5704, doi:10.1002/2014JC009915.

——, ——, and T. Tamura, 2010: Modeling sea ice production and dense shelf water formation in coastal polynyas around East Antarctica. *J. Geophys. Res.*, **115**, C10006, doi:10.1029/2010JC006133.

——, ——, and G. D. Williams, 2011a: Dense shelf water formation and brine-driven circulation in the Adélie and George V Land region. *Ocean Modell.*, **37**, 122–138, doi:10.1016/j.ocemod.2011.01.008.

——, ——, and ——, 2011b: Impact of the Mertz Glacier tongue calving on dense water formation and export. *Nat. Commun.*, **2**, 159, doi:10.1038/ncomms1156.

Lacarra, M., M.-N. Houssais, E. Sultan, S. R. Rintoul, and C. Herbaut, 2011: Summer hydrography on the shelf off Terre Adélie/George V Land based on the ALBION and CEAMARC observations during the IPY. *Polar Sci.*, **5**, 88–103, doi:10.1016/j.polar.2011.04.008.

——, ——, C. Herbaut, E. Sultan, and M. Beauverger, 2014: Dense shelf water production in the Adélie Depression, East Antarctica, 2004–2012: Impact of the Mertz Glacier calving. *J. Geophys. Res.*, **119**, 5203–5220, doi:10.1002/2013JC009124.

Legrésy, B., A. Wendt, I. Tabacco, F. Rémy, and R. Dietrich, 2004: Influence of tides and tidal current on Mertz Glacier, Antarctica. *J. Glaciol.*, **50**, 427–435, doi:10.3189/172756504781829828.

——, and Coauthors, 2010: CRAC!!! in the Mertz Glacier, Antarctica. Antarctic Climate and Ecosystems Cooperative Research Centre Rep., 10 pp. [Available online at http://www.antarctica.gov.au/__data/assets/pdf_file/0004/22549/ml_402353967939815_mertz_final_100226.pdf.]

Lemieux, J.-F., L. B. Tremblay, F. Dupont, M. Plante, G. C. Smith, and D. Dumont, 2015: A basal stress parameterization for modeling landfast ice. *J. Geophys. Res.*, **120**, 3157–3173, doi:10.1002/2014JC010678.

Leonard, B. P., M. K. MacVean, and A. P. Lock, 1993: Positivity-preserving numerical schemes for multidimensional advection. NASA Tech. Memo. 106055, 62 pp. [Available online at http://ntrs.nasa.gov/archive/nasa/casi.ntrs.nasa.gov/19930017902.pdf.]

Levitus, S., and Coauthors, 2013: World Ocean Database 1998, version 2. NOAA/NODC. [Available online at http://data.nodc.noaa.gov/cgi-bin/iso?id=gov.noaa.nodc:0098461.]

Marsland, S. J., N. L. Bindoff, G. D. Williams, and W. F. Budd, 2004: Modeling water mass formation in the Mertz Glacier polynya and Adélie Depression, East Antarctica. *J. Geophys. Res.*, **109**, C11003, doi:10.1029/2004JC002441.

——, J. A. Church, N. L. Bindoff, and G. D. Williams, 2007: Antarctic coastal polynya response to climate change. *J. Geophys. Res.*, **112**, C07009, doi:10.1029/2005JC003291.

Massom, R. A., 2003: Recent iceberg calving events in the Ninnis Glacier region, East Antarctica. *Antarct. Sci.*, **15**, 303–313, doi:10.1017/S0954102003001299.

——, P. T. Harris, K. J. Michael, and M. J. Potter, 1998: The distribution and formative processes of latent-heat polynyas in East Antarctica. *Ann. Glaciol.*, **27**, 420–426, doi:10.3198/1998AoG27-1-420-426.

——, A. B. Giles, H. A. Fricker, R. C. Warner, B. Legrésy, G. Hyland, N. Young, and A. D. Fraser, 2010: Examining the interaction between multi-year landfast sea ice and the Mertz Glacier tongue, East Antarctica: Another factor in ice sheet stability? *J. Geophys. Res.*, **115**, C12027, doi:10.1029/2009JC006083.

Mayet, C., L. Testut, B. Legrésy, L. Lescarmontier, and F. Lyard, 2013: High-resolution barotropic modeling and the calving of the Mertz Glacier, East Antarctica. *J. Geophys. Res.*, **118**, 5267–5279, doi:10.1002/jgrc.20339.

Mellor, G. L., and L. Kantha, 1989: An ice–ocean coupled model. *J. Geophys. Res.*, **94**, 10 937–10 954, doi:10.1029/JC094iC08p10937.

Nihashi, S., and K. I. Ohshima, 2015: Circumpolar mapping of Antarctic coastal polynyas and landfast sea ice: Relationship and variability. *J. Climate*, **28**, 3650–3670, doi:10.1175/JCLI-D-14-00369.1.

Noh, Y., and H. J. Kim, 1999: Simulations of temperature and turbulence structure of the oceanic boundary layer with the improved near-surface process. *J. Geophys. Res.*, **104**, 15 621–15 634, doi:10.1029/1999JC900068.

Presti, M., L. Barbara, D. Denis, S. Schmidt, L. De Santis, and X. Crosta, 2011: Sediment delivery and depositional patterns off Adélie Land (East Antarctica) in relation to late Quaternary climatic cycles. *Mar. Geol.*, **284**, 96–113, doi:10.1016/j.margeo.2011.03.012.

Rignot, E., 2002: Mass balance of East Antarctic glaciers and ice shelves from satellite data. *Ann. Glaciol.*, **34**, 217–227, doi:10.3189/172756402781817419.

——, J. L. Bamber, M. R. van den Broeke, C. Davis, Y. Li, W. J. van de Berg, and E. van Meijgaard, 2008: Recent Antarctic ice mass loss from radar interferometry and regional climate modelling. *Nat. Geosci.*, **1**, 106–110, doi:10.1038/ngeo102.

——, S. Jacobs, J. Mouginot, and B. Scheuchl, 2013: Ice-shelf melting around Antarctica. *Science*, **341**, 266–270, doi:10.1126/science.1235798.

Schodlok, M. P., D. Menemenlis, and E. J. Rignot, 2016: Ice shelf basal melt rates around Antarctica from simulations and observations. *J. Geophys. Res.*, **121**, 1085–1109, doi:10.1002/2015JC011117.

Semtner, A. J., 1976: A model for the thermodynamic growth of sea ice in numerical investigations of climate. *J. Phys. Oceanogr.*, **6**, 379–389, doi:10.1175/1520-0485(1976)006<0379:AMFTTG>2.0.CO;2.

Shadwick, E. H., and Coauthors, 2013: Glacier tongue calving reduced dense water formation and enhanced carbon uptake. *Geophys. Res. Lett.*, **40**, 904–909, doi:10.1002/grl.50178.

Shimada, K., S. Aoki, K. I. Ohshima, and S. R. Rintoul, 2012: Influence of Ross Sea Bottom Water changes on the warming and freshening of the Antarctic Bottom Water in the Australian–Antarctic Basin. *Ocean Sci.*, **8**, 419–432, doi:10.5194/os-8-419-2012.

Tamura, T., K. I. Ohshima, and S. Nihashi, 2008: Mapping of sea ice production for Antarctic coastal polynyas. *Geophys. Res. Lett.*, **35**, L07606, doi:10.1029/2007GL032903.

——, G. D. Williams, A. D. Fraser, and K. I. Ohshima, 2012: Potential regime shift in decreased sea ice production after the Mertz Glacier calving. *Nat. Commun.*, **3**, 826, doi:10.1038/ncomms1820.

——, K. I. Ohshima, A. D. Fraser, and G. D. Williams, 2016: Sea ice production variability in Antarctic coastal polynyas. *J. Geophys. Res. Oceans*, **121**, 2967–2979, doi:10.1002/2015JC011537.

Tang, S., D. Qin, J. Ren, J. Kang, and Z. Li, 2007: Structure, salinity and isotopic composition of multi-year landfast sea ice in Nella Fjord, Antarctica. *Cold Reg. Sci. Technol.*, **49**, 170–177, doi:10.1016/j.coldregions.2007.03.005.

Timmermann, R., and Coauthors, 2010: A consistent data set of Antarctic ice sheet topography, cavity geometry, and global bathymetry. *Earth Syst. Sci. Data*, **2**, 261–273, doi:10.5194/essdd-3-231-2010.

Wang, Q., S. Danilov, and J. Schröter, 2008: Comparison of overflow simulations on different vertical grids using the finite element ocean circulation model. *Ocean Modell.*, **20**, 313–335, doi:10.1016/j.ocemod.2007.10.005.

Williams, G. D., and N. L. Bindoff, 2003: Wintertime oceanography of the Adélie Depression. *Deep-Sea Res. II*, **50**, 1373–1392, doi:10.1016/S0967-0645(03)00074-2.

——, ——, S. J. Marsland, and S. R. Rintoul, 2008: Formation and export of dense shelf water from the Adélie Depression, East Antarctica. *J. Geophys. Res.*, **113**, C04039, doi:10.1029/2007JC004346.

——, S. Aoki, S. S. Jacobs, S. R. Rintoul, T. Tamura, and N. L. Bindoff, 2010: Antarctic Bottom Water from the Adélie and George V Land coast, East Antarctica (140–149°E). *J. Geophys. Res.*, **115**, C04027, doi:10.1029/2009JC005812.